AD-A118 907 OHIO STATE UNIV COLUMBUS ELECTROSCIENCE LAB F/G 9/5
THE NEAR FIELD RADIATION PATTERNS OF A SPHEROID-MOUNTED ANTENNA--ETC(U)
NOV 80 H CHUNG, W.D BURNSIDE, N WANG N00019-80-C-0050
UNCLASSIFIED ESL-712527-2 NL

1 OF 1
AD
A118907

END
DATE
FILMED
10-82
DTIC

(12)

OSU

The Ohio State University

THE NEAR FIELD RADIATION PATTERNS OF A SPHEROID-MOUNTED ANTENNA

H. Chung, W.D. Burnside, and N. Wang

The Ohio State University
ElectroScience Laboratory
Department of Electrical Engineering
Columbus, Ohio 43212

Quarterly Report 712527-2
Contract N00019-80-C-0050
November 1980

Department of the Navy
Naval Air Systems Command
Washington, D.C. 20361

NOTICES

UNCLASSIFIED
SECURITY CLASSIFICATION OF THIS PAGE (When Data Entered)

REPORT DOCUMENTATION PAGE

READ INSTRUCTIONS
BEFORE COMPLETING FORM

1. REPORT NUMBER
2. GOVT ACCESSION NO. A118907
3. RECIPIENT'S CATALOG NUMBER

4. TITLE (and Subtitle)
THE NEAR FIELD RADIATION PATTERNS OF A
SPHEROID-MOUNTED ANTENNA

5. TYPE OF REPORT & PERIOD COVERED
Quarterly Report
2/29/79 - 5/29/80

6. PERFORMING ORG. REPORT NUMBER
ESL 712527-2

7. AUTHOR(s)
H. Chung
W. D. Burnside
N. Wang

8. CONTRACT OR GRANT NUMBER(s)
Contract N00019-80-C-0050

9. PERFORMING ORGANIZATION NAME AND ADDRESS
The Ohio State University ElectroScience
Laboratory, Department of Electrical
Engineering, Columbus, Ohio 43212

10. PROGRAM ELEMENT, PROJECT, TASK AREA & WORK UNIT NUMBERS

11. CONTROLLING OFFICE NAME AND ADDRESS
Department of the Navy
Naval Air Systems Command
Washington, D.C. 20361

12. REPORT DATE
November 1980

13. NUMBER OF PAGES
60

14. MONITORING AGENCY NAME & ADDRESS(if different from Controlling Office)

15. SECURITY CLASS. (of this report)
Unclassified

15a. DECLASSIFICATION/DOWNGRADING SCHEDULE

16. DISTRIBUTION STATEMENT (of this Report)

APPROVED FOR PUBLIC RELEASE;
DISTRIBUTION UNLIMITED

17. DISTRIBUTION STATEMENT (of the abstract entered in Block 20, if different from Report)

18. SUPPLEMENTARY NOTES

19. KEY WORDS (Continue on reverse side if necessary and identify by block number)

Electromagnetic radiation
High frequency solutions
Geometrical Theory of Diffraction
Perturbation Methods
Near Field Solution
Prolate spheroid mounted antenna

20. ABSTRACT (Continue on reverse side if necessary and identify by block number)

An efficient numerical solution for the high frequency near field radiation patterns of a spheroid-mounted antenna is investigated. The Geometrical Theory of Diffraction is the basic approach applied here. The ray analysis in the lit region is straightforward; whereas, the geodesic paths on the surface dictate whether the shadow region solution is practical to obtain or not. Previous attempts employing calculus of variations or tensor analysis were too complicated to use. Cylinder

DD FORM 1 JAN 73 1473 EDITION OF 1 NOV 65 IS OBSOLETE

UNCLASSIFIED
SECURITY CLASSIFICATION OF THIS PAGE (When Data Entered)

20.

and cone perturbation methods are presented to simulate the geodesic paths on a spheroid, which in turn can be used to model an aircraft or missile fuselage. The geodesic paths are then efficiently solved via a numerical approach, in that a cylinder and cone are developed surfaces.

This study has presented a very useful solution in approximating the geodesic paths on a spheroid, and predicting the high frequency near field radiation patterns for spheroid-mounted antennas. Using this perturbation approach one can extend this technique to solve for the geodesic paths on more complex convex surfaces.

CONTENTS

I. INTRODUCTION

The object of this study is to develop an efficient numerical solution for the high-frequency near zone radiation patterns of a spheriod-mounted antenna. The Geometrical Theory of Diffraction (GTD) is employed for the pattern calculation of which the creeping wave [1] solution in the shadow region is of particular interest here. According to the generalized Fermat's principle, a ray emanating from a source, which is located on the surface, follows a geodesic path on the surface and continually sheds energy into the shadow region. Such a creeping wave mechanism is illustrated in Figure 1(a), from which it can be seen that a ray traverses from the source point Q' to the diffraction point Q, and then propagates along the geodesic tangent at Q toward the observation point P_s. Since most parameters involved in the pattern calculation are related to the ray path, the geodesic solution on the surface for a near zone field point constitutes a major portion of this study.

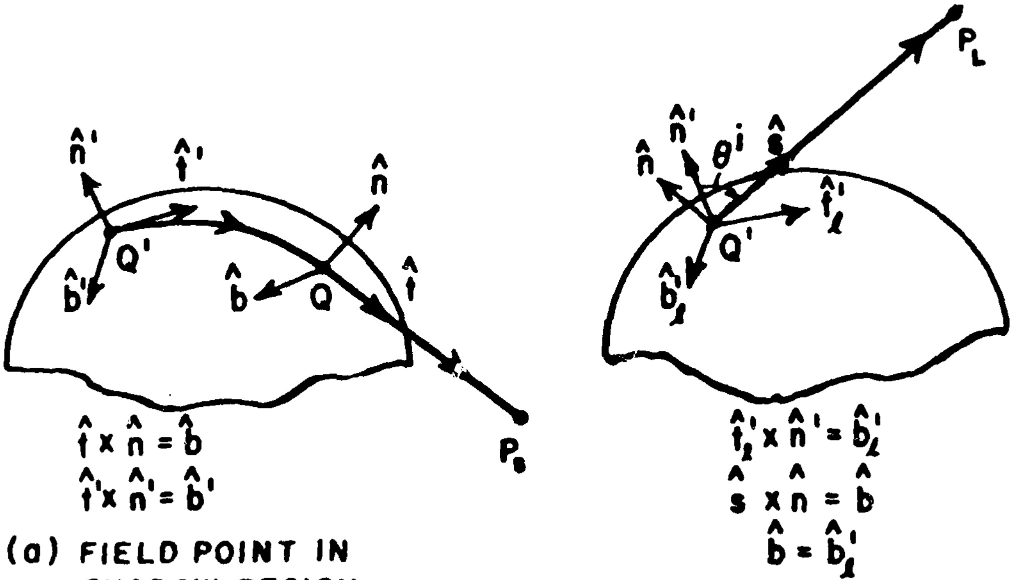

(a) FIELD POINT IN SHADOW REGION

(b) FIELD POINT IN LIT REGION

Figure 1. Ray paths in the shadow and lit regions.

The spheroid is studied because of its three dimensional nature in that it can be used to simulate an aircraft or missile fuselage. For a flush-mounted airborne antenna, the fuselage has a dominant effect on the resulting radiation pattern. Previously [2] the fuselage was simulated by an elliptic cylinder; however, the cylinder model could not predict the pattern close to the nose or tail sectors, where the deviation from the physical situation becomes very prominent. Previous attempts [2], using the spheroid model, employed calculus of variations or tensor analysis to calculate the geodesic paths. The resulting algorithms were very time-consuming and virtually impractical to use. Therefore, a perturbation method is presented here in an attempt to combine the simplicity of the cylinder or cone solution with the generality of the prolate spheroid.

Before examining our perturbation approach, it is appropriate to study the basic radiation mechanisms in some detail in that they suggest the present solution. The ray analysis in the lit region can be rather straightforwardly analyzed for any convex surface; however, the geodesics which are necessary to treat the shadow region dictate what surfaces can be efficiently analyzed. In the shadow region, the energy propagates outward from the source along the geodesic paths. As the energy flows around the surface, it is continuously diffracted along the geodesic tangent toward the field point such that the significant effect of the surface is associated with a region around the source. In fact, for a prolate spheroid, the significant portion of the surface, which is associated with the dominant energy, may look as shown in Figure 2. Note that this region can be specified by following the various geodesic paths until the radiation level along a given path becomes insignificant, i.e., more than 40 dB below the pattern maximum. With this in mind, it is clear that one could represent the prolate spheroid by a structure which simulates the circular cross-section completely; however, the profile (i.e., the elliptic curve) could be approximated by a simpler shape in that the significant energy region does not cover a large portion of the profile shape. Consequently, a right circular cone perturbation

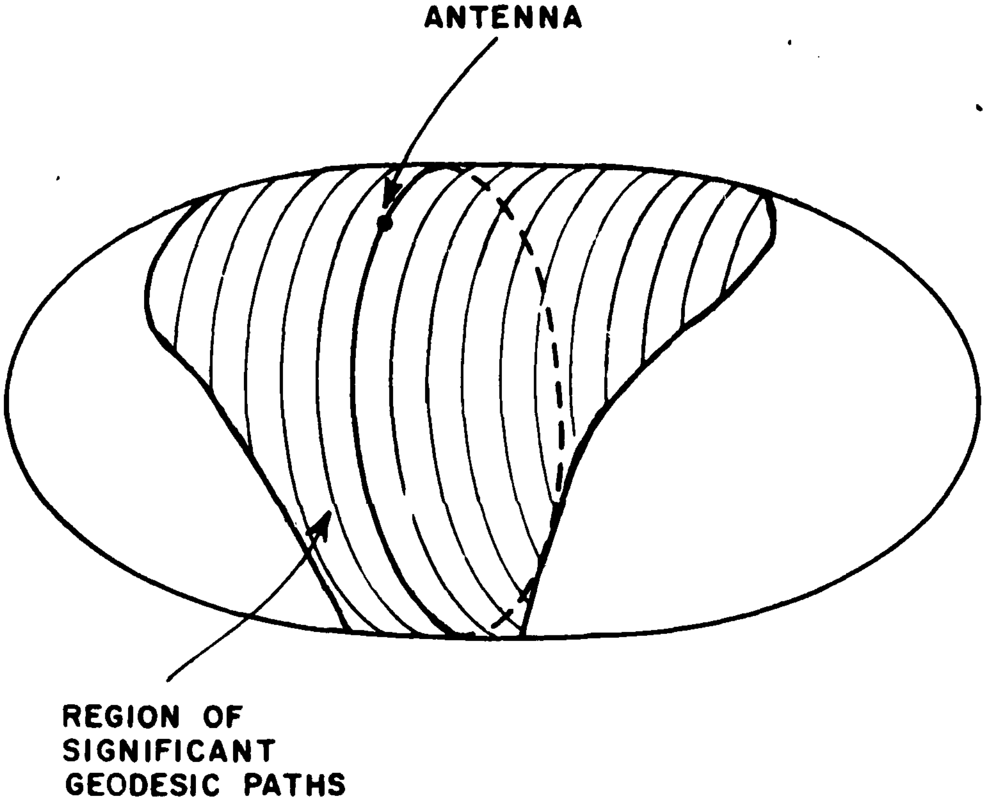

Figure 2. The region of significant energy flow from an antenna mounted on a prolate spheroid.

is chosen here to simulate the spheroid which in turn can be used to model a fuselage. This perturbation model is illustrated in Figure 3 for a source located near one end of the spheroid. Note that if the antenna is placed at the center of the spheroid, the cone actually becomes a right circular cylinder.

In that the cone is a developed surface, one can unfold the cone such that a planar structure results. The geodesics associated with the cone are, then, straight lines on this planar structure. In order to allow for a geodesic solution between the simplicity of the cone and the rigor of the spheroid, one can perturb the cone by bending it along its generator as illustrated in Figure 3(b). In that a perturbation technique is employed, the geodesic paths for the cone are simply modified such that the solution for the spheroid is basically straightforward and is the basis for this report. It is obvious that one cannot use this perturbation if significant energy propagates great distances along the surface. However, as discussed above, the energy which propagates great distances along the spheroid generator becomes insignificant in magnitude such that one need not solve for the true geodesic paths outside the region shown in Figure 3. The simplicity of these perturbed geodesic paths allows one to very efficiently determine the significant ray paths on the prolate spheroid.

It is noted that, since GTD is a high-frequency method, the lower frequency limit of this solution is dictated by the electrical dimensions of the spheroid, i.e., the semi-minor axis of the spheroid is required to be at least a wavelength.

The curved surface diffraction solutions employed here are briefly discussed in Section II. The parameters needed for this GTD solution are described in Section III in terms of the cylinder and cone perturbations for near field used to simulate the geodesic paths on the spheroid. Computational results are presented in Section IV. Finally, a summary of this study is made in Section V.

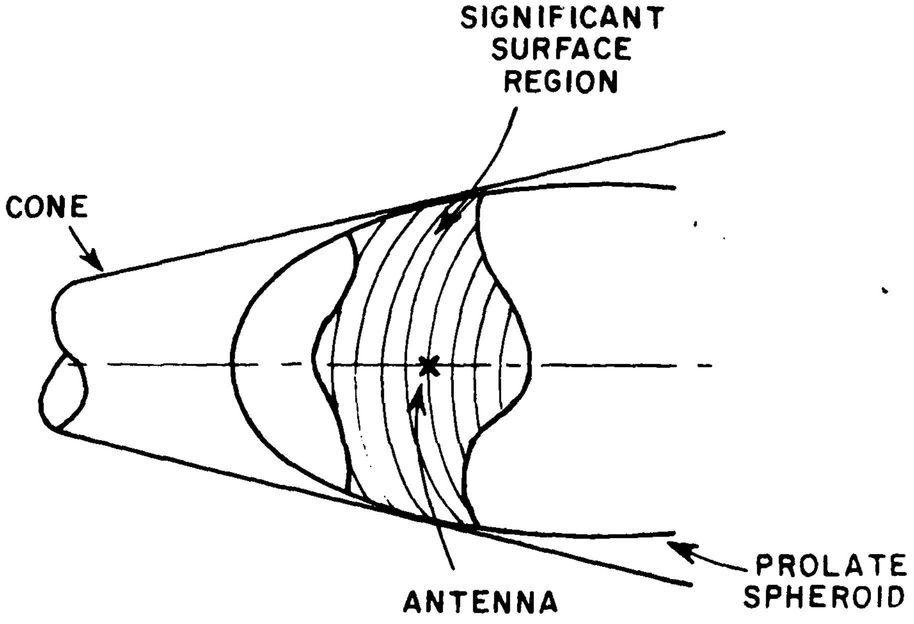

Figure 3(a). Cone simulation.

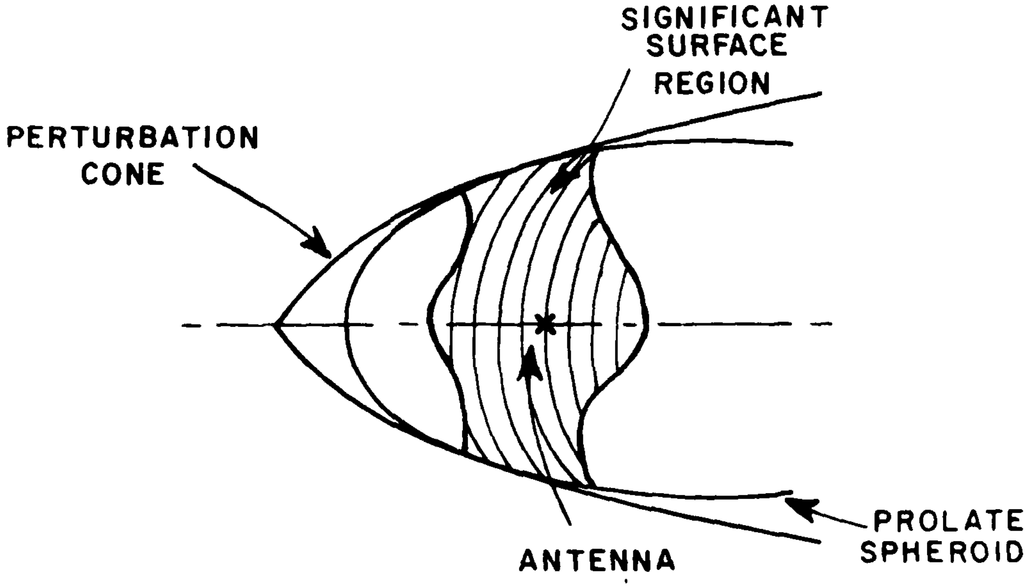

Figure 3(b). Cone perturbation model.

II. THEORETICAL BACKGROUND

A. Introduction

The radiated field of a spheroid-mounted antenna is analyzed using the Geometrical Theory of Diffraction (GTD). The surface is assumed to be perfectly conducting, and the surrounding medium is free space. An exp $(j\omega t)$ time dependence is understood and suppressed in the following formulations.

Consider an infinitesimal, magnetic current moment $d\overline{P}_m(Q')$ or an electric current moment $d\overline{P}_e(Q')$ located on a perfectly conducting convex surface as shown in Figure 1; the sources

$$dP_m(Q') = \overline{E}(Q') \times \hat{n}' da' \quad \text{and} \quad d\overline{P}_e(Q') = I(\ell')d\ell'\hat{n}'$$

pertain to the aperture and monopole type excitations with

$\overline{E}(Q')$ = electric field at Q',

$\hat{n}'$ = outward unit surface normal at Q',

da' = area element at Q',

$I(\ell')$ = electric current distribution on the monopole, and

ℓ' = distance parameter along the monopole.

According to geometrical optics, the space surrounding the source is divided into an illuminated and shadow region by a plane tangent to the surface at Q'. This plane is referred to as a shadow boundary. Since the field in the deep lit region is essentially that obtained from geometrical optics, and the field in the deep shadow region is relatively weak, the solution for the transition region adjacent to the shadow boundary is of more interest and discussed below.

B. Shadow Region

The creeping wave mechanism in the shadow region is illustrated in Figure 4. From the generalized Fermat's principle, a ray emanating from the source $d\bar{P}^{m}_{e}(Q')$ at Q' traverses a geodesic path Q'Q on the surface, and propagates along the geodesic tangent at Q toward the field point P_s. The field $d\bar{E}^{m}_{e}$ at P_s can be expressed in terms of the field at a reference point P_0 by [1]

$$d\bar{E}^{m}_{e}(P_s) \sim d\bar{E}^{m}_{e}(P_0)\sqrt{\frac{\rho_1^d \rho_2^d}{(\rho_1^d+s_0)(\rho_2^d+s_0)}}\; e^{-jks_0} + O[m^{-2}, m^{-3}] \qquad (1)$$

where

ρ_1^d and ρ_2^d are the principal radii of curvatures of the wavefront

and $O[m^{-2}, m^{-3}, \ldots]$ are the higher order terms.

From Figure 4, it is seen that if the reference point P_0 is moved to the curved surface diffraction point Q, then $\rho_1^d \to 0$, $\rho_2^d \to \rho_c$, and $s_0 \to s$. Since $d\bar{E}^{m}_{e}(P_s)$ is independent of the reference point P_0, it follows that

$$\lim_{\substack{P_0 \to Q \\ \rho_1^d \to 0}} \sqrt{\rho_1^d}\; d\bar{E}^{m}_{e}(P_0) = \bar{L}^{m}_{e}(Q', Q) \; ; \qquad (2)$$

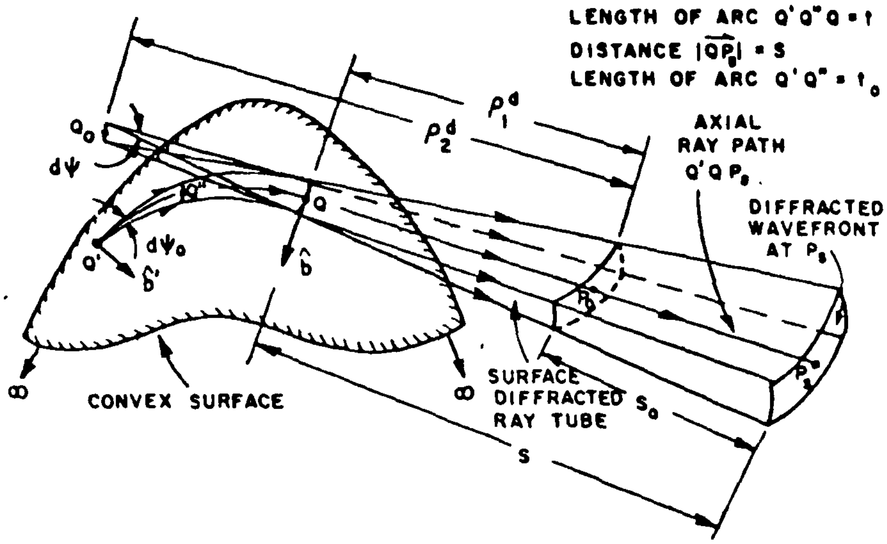

(a) Perspective view of a surface diffracted ray tube (enlarged view).

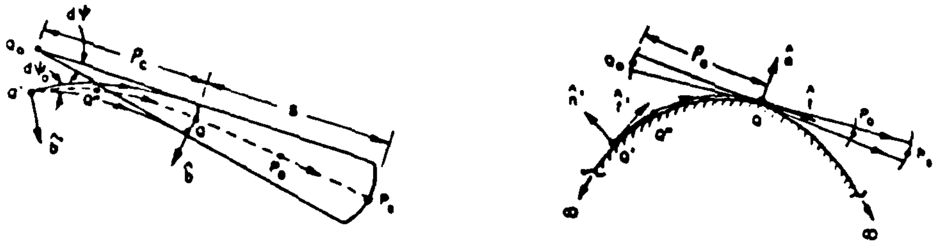

(b) Top view of diffracted ray tube indicating the divergence of the rays and the unit binormal vectors at Q' and Q.

(c) Side view of surface diffracted ray tube and the unit normal and tangent vectors at Q' and Q.

Figure 4. Surface diffracted ray tube and ray coordinates for the shadow region.

then

$$d\bar{E}_{\substack{m\\e}}(Ps) \sim \bar{L}_{\substack{m\\e}}(Q',Q)\sqrt{\frac{\rho_c}{s(\rho_c+s)}}\ e^{-jks}\ . \tag{3}$$

Furthermore, $\bar{L}_{\substack{m\\e}}(Q',Q)$ can be related to the source strength $d\bar{P}_{\substack{m\\e}}$ at Q' by

$$\bar{L}_{\substack{m\\e}}(Q',Q) = d\bar{P}_{\substack{m\\e}}(Q') \cdot \bar{\bar{T}}_{\substack{m\\e}}(Q',Q) \tag{4}$$

where $\bar{\bar{T}}_{\substack{m\\e}}(Q',Q)$ is given by [1]

$$\bar{\bar{T}}m(Q',Q) = \frac{-jk}{4\pi}\left[\hat{b}'\hat{n}T_1(Q')H+\hat{t}'\hat{b}T_2(Q')S+\hat{b}'\hat{b}T_3(Q')S+\hat{t}'\hat{n}T_4(Q')H\right]$$

$$e^{-jkt}\sqrt{\frac{d\psi_o}{d\eta(Q)}}\left(\frac{\rho_g(Q)}{\rho_g(Q')}\right)^{1/6} \tag{5}$$

$$\bar{\bar{T}}e\,(Q',Q) = \frac{-jkZo}{4\pi}\left[\,\hat{n}'\hat{n}T_5(Q')H+\hat{n}'\hat{b}T_6(Q')S\,\right]e^{-jkt}$$

$$\sqrt{\frac{d\psi_o}{d\eta(Q)}}\left(\frac{\rho_g(Q)}{\rho_g(Q')}\right)^{1/6} \tag{6}$$

Here $(\hat{t}',\hat{n}',\hat{b}')$ and $(\hat{t},\hat{n},\hat{b})$ are the *tangent, normal and binormal unit* vectors to the surface at the source point (Q') and diffraction point (Q), respectively. As seen from Figure 4, $\hat{t}\times\hat{n}=\hat{b}$ and $\hat{t}'\times\hat{n}'=\hat{b}'$. The quantities $T_1(Q'),\ldots,T_6(Q')$ are the torsion factors at Q' and are given in Table I. Also,

$$H = g(\xi) \tag{7}$$

$$S = \frac{-j}{m(Q')}\mathcal{G}(\xi) \tag{8}$$

TABLE I (FOR SHADOW REGION)

TYPE OF CONVEX SURFACE	SLOT OR $d\bar{p}_m$ CASE				MONOPOLE OR $d\bar{p}_e$ CASE		SURFACE RAY TORSION	SURFACE RADIUS OF CURVATURE IN $\hat{t}'$ DIRECTION	SURFACE DIFFRACTED RAY CAUSTIC DISTANCE
	$T_1(Q')$	$T_2(Q')$	$T_3(Q')$	$T_4(Q')$	$T_5(Q')$	$T_6(Q')$	$T(Q')$	$\rho_g(Q)$	ρ_c
SPHERE	1	1	0	0	1	0	0	a	$a \tan(\frac{t}{a})$
CIRCULAR CYLINDER	1	1	$\frac{\sin 2\alpha'}{2a} \cdot \frac{a}{\sin^2 \alpha'}$	0	1	$\frac{\sin 2\alpha'}{2a} \cdot \frac{a}{\sin^2 \alpha'}$	$\frac{\sin 2\alpha'}{2a}$	$\frac{a}{\sin^2 \alpha'}$	∞
ARBITRARY CONVEX SURFACE	1	1	$T(Q')\rho_g(Q')$	0	1	$T(Q')\rho_g(Q')$	$\frac{\sin 2\alpha'}{2}\left(\frac{1}{R_2(Q')} - \frac{1}{R_1(Q')}\right)$ WITH $R_1(Q') \geq R_2(Q')$	$\left(\frac{\cos^2\alpha'}{R_1(Q')} + \frac{\sin^2\alpha'}{R_2(Q')}\right)^{-1}$	$\frac{2\sqrt{E}\,G}{\partial G/\partial t}$

ote: (1) α' is defined by $\hat{\tau}_1' \cdot \hat{t}' = \cos\alpha'$ where $\hat{\tau}_1'$ is the principal direction unit vector associated with $R_1(Q')$.

(2) The quantities E and G denote two of the three coefficients E, F, G that appear in the "first fundamental form" of Differential Geometry [3].

with

$$g(\xi) = \frac{1}{\sqrt{\pi}} \int_{\infty \exp(-j2\pi/3)}^{\infty} d\tau \, \frac{\exp(-j\tau\xi)}{w_2'(\tau)} \quad \text{and} \tag{9}$$

$$\tilde{g}(\xi) = \frac{1}{\sqrt{\pi}} \int_{\infty \exp(-j2\pi/3)}^{\infty} d\tau \, \frac{\exp(-j\tau\xi)}{w_2(\tau)} \tag{10}$$

which are known as the acoustic hard and soft Fock functions. The Fock type Airy function is given by

$$w_2(\tau) = \frac{1}{\sqrt{\pi}} \int_{\infty \exp(j2\pi/3)}^{\infty} dt \cdot \exp(\tau t - t^3/3) \tag{11}$$

and $w_2'(\tau)$ is the derivative of $w_2(\tau)$ with respect to τ. The Fock parameter ξ for the shadow region is given by [1]

$$\xi = \int_{Q'}^{Q} dt' \, \frac{m(t')}{\rho_g(t')} \tag{12}$$

with

$$m(t') = \left[\frac{k\rho_g(t')}{2} \right]^{1/3} . \tag{13}$$

Here $\rho_g(t')$ is the surface radius of curvature along the ray path at t'. The width of the surface ray tube at Q, $d\eta(Q)$, is given by

$$d\eta(Q) = \rho_c d\psi . \tag{14}$$

The parameters Z_0 and t are defined as the free space wave impedance and geodesic arc length from Q' to Q, respectively.

Combining Equations (3)-(14), the n and b directed components of $dE^{m}_{e}(P_s)$ are given by [1]

(a) $d\bar{P}m(Q')$ case:

$$dE_m^n(P_s) = \frac{-jk}{4\pi} (d\bar{P}m \cdot \hat{b}')He^{-jkt}\left[\frac{\rho_g(Q')}{\rho_g(Q)}\right]^{-1/6} \sqrt{\frac{d\psi_o}{d\psi}} \sqrt{\frac{1}{s(\rho_c+s)}}$$

$$e^{-jks} + O[m^{-2}] \tag{15}$$

$$dE_m^b(P_s) = \frac{-jk}{4\pi} [(d\bar{P}m \cdot \hat{b})T_o S + (d\bar{P}m \cdot \hat{t}')S] e^{-jkt}\left[\frac{\rho_g(Q')}{\rho_g(Q)}\right]^{-1/6}$$

$$\sqrt{\frac{d\psi_o}{d\psi}} \sqrt{\frac{1}{s(\rho_c+s)}} \quad e^{-jks} + O\left[m^{-2}, m^{-3}\right] \tag{16}$$

(b) $d\bar{P}_e(Q')$ case:

$$dE_e^n(Ps) = \frac{-jkZ_o}{4\pi} dP_e(Q')He^{-jkt}\left[\frac{\rho_g(Q')}{\rho_g(Q)}\right]^{-1/6} \sqrt{\frac{d\psi_o}{d\psi}} \sqrt{\frac{1}{s(\rho_c+s)}}$$

$$e^{-jks} + O[m^{-2}] \tag{17}$$

$$dE_e^b(P_s) = \frac{-jkZ_o}{4\pi} dP_e(Q')T_o S e^{-jkt}\left[\frac{\rho_g(Q')}{\rho_g(Q)}\right]^{-1/6} \sqrt{\frac{d\psi_o}{d\psi}} \sqrt{\frac{1}{s(\rho_c+s)}}$$

$$e^{-jks} + O[m^{-2}] \tag{18}$$

where $To=T(Q')\rho_g(Q')$ with $T(Q')$ being the surface torsic.. at the source location (refer to Table 1).

C. Lit Region

From geometrical optics, the source $d\bar{P}^{m}_{e}(Q')$ at Q' excites waves which propagate along straight line ray paths from the source to field point in the lit region. As shown in Figure 5, the field $d\bar{E}^{m}_{e}(P_L$ at point P_L is expressed by

$$d\bar{E}^{m}_{e}(P_L) \backsim d\bar{E}^{m}_{e}(\tilde{P}_o)\sqrt{\frac{\rho_1^i\rho_2^i}{(\rho_1^i+\tilde{s}_o)(\rho_2^i+\tilde{s}_o)}}\; e^{-jk\tilde{s}_o}+O\left[m_\ell^{-2},m_\ell^{-3}\right] \tag{19}$$

Since Q' is the only caustic of the incident rays, the principal radii of curvature ρ_1^i and ρ_2^i associated with the incident wavefront at $\tilde{P}_o$ are identical, i.e., $\rho_1^i = \rho_2^i$. Furthermore, $d\bar{E}^{m}_{e}(P_L)$ is independent of the reference point $\tilde{P}_o$. If $\tilde{P}_o$ is chosen to be at Q', it follows that

$$\lim_{\substack{\tilde{P}_o\to Q'\\ \rho i\to 0\\ \tilde{s}_o\to s}} \rho^i d\bar{E}^{m}_{e}\,(Po) = \bar{L}^{\ell}_{\substack{m\\e}} \tag{20}$$

should exist. Thus, $\bar{L}^{\ell}_{\substack{m\\e}}$ can be related to $d\bar{P}^{m}_{e}(Q')$ by [1]

$$\bar{L}^{\ell}_{\substack{m\\e}} = d\bar{P}^{m}_{e}(Q')\cdot\bar{\bar{T}}^{\ell}_{\substack{m\\e}} \tag{21}$$

Equations (19)-(21) are, then, combined to yield

$$d\bar{E}^{m}_{e}(P_L) \backsim d\bar{P}^{m}_{e}(Q')\cdot\bar{\bar{T}}^{\ell}_{\substack{m\\e}}\cdot\frac{e^{-jks}}{s}+O[m_\ell^{-2},m_\ell^{-3},\dots] \tag{22}$$

$$\bar{\bar{T}}^{\ell}_{m} = \frac{-jk}{4\pi}\,[\hat{b}_\ell'\hat{n}A+\hat{t}_\ell'\hat{b}B+\hat{b}'\hat{b}_\ell C+\hat{t}_\ell'\hat{n}D] \tag{23}$$

$$\bar{\bar{T}}^{\ell}_{e} = \frac{-jkZ_o}{4\pi}\,[\hat{n}'\hat{n}M+\hat{n}'\hat{b}N] \tag{24}$$

with A, B, C, D, M, and N are defined in Table 2. Note that $d\bar{E}^{m}_{e}(P_L)$ is decoupled into $\hat{n}$ and $\hat{b}$ components as follows:

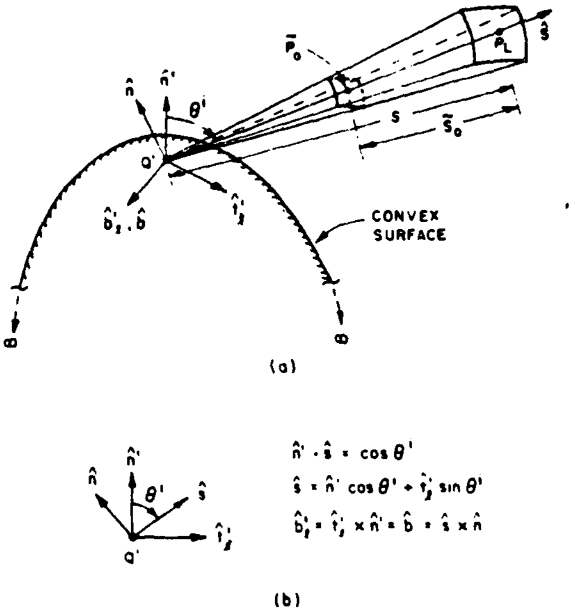

$$\hat{n}' \cdot \hat{s} = \cos\theta'$$

$$\hat{s} = \hat{n}' \cos\theta' + \hat{t}_\ell' \sin\theta'$$

$$\hat{b}_\ell' = \hat{t}_\ell' \times \hat{n}' = \hat{b} = \hat{s} \times \hat{n}$$

Figure 5. Ray tube and ray coordinates.

TABLE II (FOR LIT REGION)

SLOT OR $d\hat{p}_m$ CASE				MONOPOLE OR $d\hat{p}_e$ CASE			
A	B	C	D	M	N	T_0	F
$M^2+T_0^2F\cos\theta'$	$S^2-T_0^2F\cos^2\theta'$	T_0F	$T_0F\cos\theta'$	$\sin\theta'\left[M^2+T_0^2F\cos\theta'\right]$	$\sin\theta' T_0F$	$T(Q')\rho_g(Q')$	$\frac{S^2-M^2\cos\theta'}{1+T_0^2\cos\theta'}$

(a) $d\overline{P}_m(Q')$ case:

$$dE^n_m(P_L) = \frac{-jk}{4\pi}[(d\overline{P}_m \cdot \hat{b}')(H^\ell + T^2_o F\cos\theta^i) + (d\overline{P}_m \cdot \hat{t}')T_o F\cos\theta^i]$$

$$\frac{e^{-jks}}{s} + O[m_\ell^{-2}] \tag{25}$$

$$dE_m(P_L) = \frac{-jk}{4\pi}[\,(d\overline{P}_m \cdot \hat{b}')T_o F + (d\overline{P}_m \cdot \hat{t}')(S^\ell - T^2_o F\cos^2\theta^i)]$$

$$\frac{e^{-jks}}{s} + O[m_\ell^{-2}, m_\ell^{-3}] \tag{26}$$

(b) $d\overline{P}_e(Q')$ case:

$$dE^n_e(P_L) = \frac{-jkZ_o}{4\pi}\; dP_e(Q')\sin\theta^i\,[H^\ell + T^2_c F\cos\theta^i]\,\frac{e^{-jks}}{s} + O[m_\ell^{-2}] \tag{27}$$

$$dE^b_e(P_L) = \frac{-jkZ_o}{4\pi}\; dP_e(Q')\sin\theta^i T_o F\,\frac{e^{-jks}}{s} + O[m_\ell^{-2}] \tag{28}$$

where

$$H^\ell = g(\xi_\ell)e^{-j\,\xi_\ell^3/3} \tag{29}$$

$$S^\ell = \frac{-j}{m_\ell(Q')}\;\tilde{g}(\xi_\ell)e^{-j\,\xi_\ell^3/3} \tag{30}$$

and

$$\xi_\ell = -m_\ell(Q')\cos\theta^i \tag{31}$$

$$m_\ell(Q') = \frac{m(Q')}{(1+T_0^2\cos^2\theta^i)^{1/3}} \tag{32}$$

The angle θ^i is defined by $\hat{n}'\cdot\hat{s} = \cos\theta^i$ as shown in Figure 5. Also,

$$F = \frac{S^\ell - H^\ell\cos\theta^i}{1+T_0^2\cos^2\theta^i} \tag{33}$$

as defined in Table II.

D. Pattern Factors

The solutions for short magnetic or electric dipoles have been given in parts B and C. One approach to analyze an extended aperture or linear antenna problem is to integrate the above solutions over the source distribution, if it is known. This is an application of the superposition theorem, and one approximates the source distribution by an array of short magnetic (or electric) dipoles on the conducting surface. This is an accurate solution, however, rather tedious. A more efficient approach is to modify $d\bar{P}_e^m(Q')$ such that

(a) in the shadow region:

$$\bar{P}_m = \hat{p}_m \frac{2B}{\pi}\left[\frac{\cos\left(\frac{kB}{2}\,(\hat{p}_m\cdot\hat{t}')\right)}{1-\left(\frac{kB}{\pi}(\hat{p}_m\cdot\hat{t}')\right)^2}\right]\left[\frac{\sin\left(\frac{kA}{2}\,\hat{p}_m\,\hat{b}'\right)}{\frac{kA}{2}\hat{p}_m\cdot\hat{b}'}\right]$$

$$\bar{P}_e = \hat{n}'\left[1-\cos(kL)\right] \tag{35}$$

(b) in the lit region:

$$\overline{P}_m = \hat{p}_m \frac{2B}{\pi} \left[\frac{\cos\left(\frac{kB}{2}\sin\theta^i(\hat{P}_m \cdot \hat{t}')\right)}{1-\left(\frac{kB}{\pi}\sin\theta^i(\hat{P}_m \cdot \hat{t}')\right)^2} \right] \left[\frac{\sin \frac{kA}{2} \sin\theta^i(\hat{P}_m \cdot \hat{b}')}{\frac{kA}{2} \sin\theta^i(\hat{P}_m \cdot \hat{b}')} \right] \tag{36}$$

$$\overline{P}_e = \hat{n}' \frac{\cos(kL\hat{n}' \cdot \hat{s}) - \cos(kL)}{1-(\hat{n}' \cdot \hat{s})^2} \tag{37}$$

Here $\hat{P}_m$ = unit vector in the direction of magnetic current moment,

A,B = the length of the short and long sides of the slot, and

L = the length of the monopole.

It is noted that L is not to exceed a quarter wavelength for the solutions to be valid.

III. NUMERICAL TECHNIQUE AND PERTURBATION METHOD

A. Introduction

It is seen that, for an antenna mounted on a spheroid, the solution in the lit region is relatively straightforward. On the other hand, the geodesic paths associated with the GTD solution in the shadow region are extremely complex. Previous studies [2] employed calculus of variations or tensor analysis to calculate the geodesic paths which resulted in very inefficient solutions. An efficient numerical approach is examined in this chapter with the spheroid simulated by a perturbed cone or cylinder model. In that the cone and cylinder are developed surfaces for which the geodesics are efficient to solve. Given a radiation direction (θ_t, ϕ_t), one can find the final diffraction point (θ_Q, ϕ_Q)

by following the geodesic path, step by step, until the geodesic tangent coincides with (θ_t,ϕ_t). This is a rather tedious and time consuming process if applied for each new radiation direction. Considering that a new radiation direction does not deviate greatly from the previous direction, one should be able to develop a solution which uses the properties of the surface and the previous geodesic path to find the new diffraction point. Such an approach is applied here to make this solution as efficient as possible.

Since the field decays exponentially along the ray path on the surface, it is assumed that only one or possibly two dominant rays exist in the problems treated.

B. Spheroid Surface Parameters

Using the spheroid geometry shown in Figure 6, the surface is defined by

$$\vec{R}(\theta,\phi) = R(\theta)\sin\theta\cos\phi\hat{x}+R(\theta)\sin\theta\sin\phi\hat{y} + R(\theta)\cos\theta\hat{z} \tag{38}$$

with

$$R(\theta) = \frac{ab}{\sqrt{a^2\cos^2\theta+b^2\sin^2\theta}} \tag{39}$$

or

$$\vec{R}(\nu,\phi) = a\cos\nu\cos\phi\hat{x} + a\cos\nu\sin\phi\hat{y} + b\sin\nu\hat{z} \tag{40}$$

with

$$\tan\nu = \frac{b\cos\theta}{a\sin\theta} \quad . \tag{41}$$

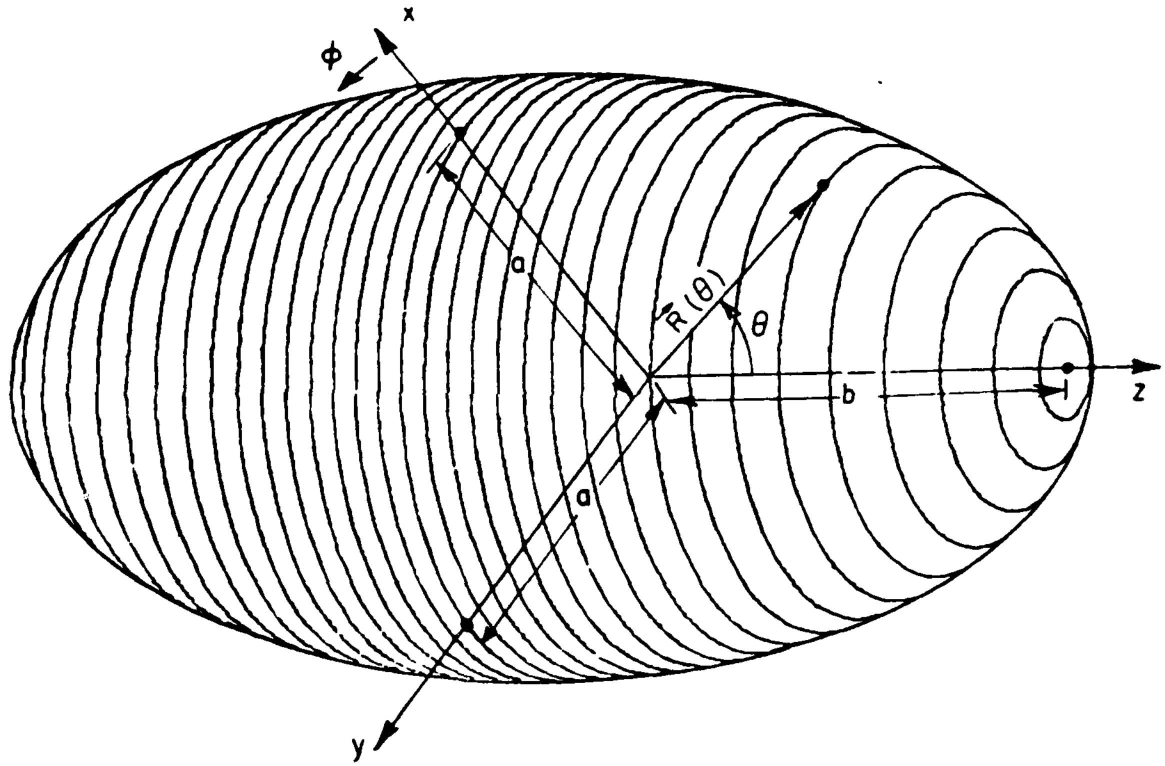

Figure 6. Geometry of spheroid.

The "ν" parameter is introduced because of its convenience in analyzing elliptic geometries.

Considering a ray which propagates along a geodesic path Q'Q on the spheroidal surface as shown in Figure 7 the three unit vectors $\hat{t}$, $\hat{n}$ and $\hat{b}$ are, as defined earlier, the geodesic tangent, outward surface normal and binormal at any point along the geodesic path. The outward surface unit normal ($\hat{n}$) is obtained from

$$\hat{n} = \frac{\vec{R}\phi \mathrm{x} \vec{R}\nu}{|\vec{R}\phi \mathrm{x} \vec{R}\nu|} \tag{42}$$

where

$$\frac{\partial\vec{R}}{\partial\nu} = \vec{R}\nu = -a\ \sin\nu\cos\phi\hat{x} - a\ \sin\nu\sin\phi\hat{y} + b\ \cos\nu\hat{z}$$

and

$$\frac{\partial\vec{R}}{\partial\phi} = \vec{R}\phi = -a\ \cos\nu\sin\phi\hat{x} + a\ \cos\nu\cos\phi\hat{y}$$

Then, the unit normal vector is given by

$$\hat{n} = \frac{b\ \cos\nu\cos\phi\hat{x} + b\ \cos\nu\sin\phi\hat{y} + a\ \sin\nu\hat{z}}{\sqrt{a^2\sin^2\nu + b^2\cos^2\nu}} \ . \tag{43}$$

The normal curvatures κ_n on the surface are evaluated by introducing the first and second fundamental forms of differential geometry [3] such that

$$\kappa_n = \frac{Ld\phi^2 + 2Md\phi d\nu + Nd\nu^2}{Ed\phi^2 + 2Fd\phi d\nu + Gd\nu^2} \tag{44}$$

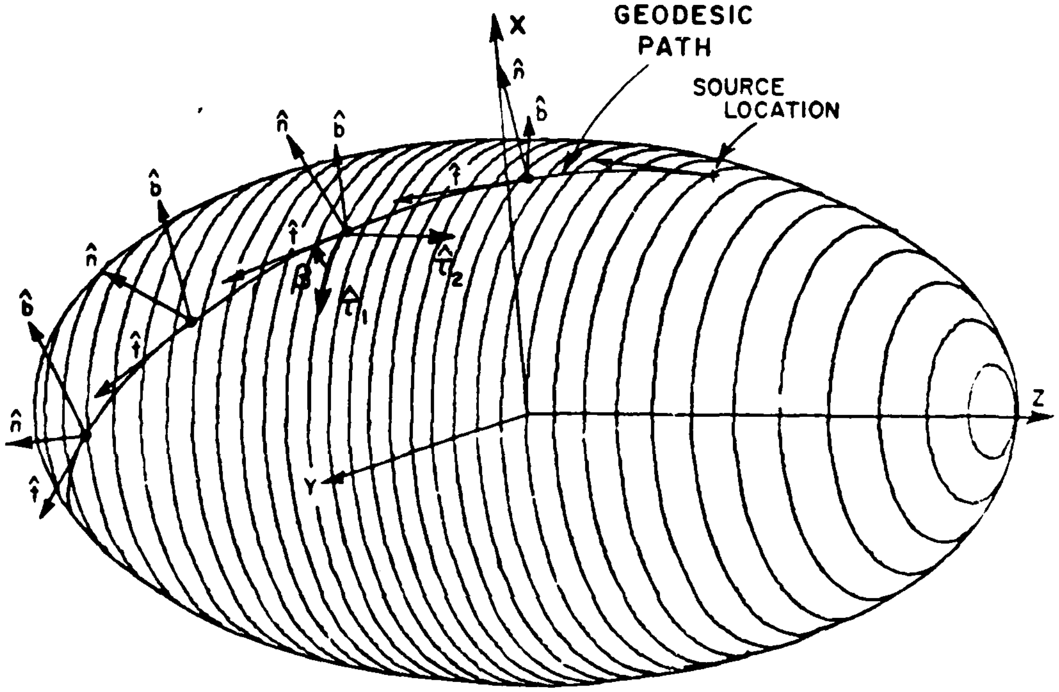

Figure 7. Geodesic path on a spheroid.

where

$$L = \vec{R}_{\phi\phi}\cdot\vec{N},\ M = \vec{R}_{\phi\nu}\cdot\vec{N},\ \text{and } N = \vec{R}_{\nu\nu}\cdot\vec{N};$$

$$E = \vec{R}_{\phi}\cdot\vec{R}_{\phi},\ F = \vec{R}_{\phi}\cdot\vec{R}_{\nu},\ \text{and } G = \vec{R}_{\nu}\cdot\vec{R}_{\nu};$$

and

$$\vec{N} = -\hat{n}\ .$$

It can be shown that

$$\vec{R}_{\phi\phi} = -a\cos\nu\cos\phi\hat{x} - a\cos\sin\phi\hat{y}\ ,$$

$$\vec{R}_{\phi\nu} = a\sin\nu\sin\phi\hat{x} - a\sin\nu\cos\phi\hat{y}\ , \text{ and}$$

$$\vec{R}_{\nu\nu} = -a\cos\nu\cos\phi\hat{x} - a\cos\nu\sin\phi\hat{y} - b\sin\nu\hat{z}.$$

After some algebraic manipulation, one obtains

$$L = ab\cos^2\nu/\sqrt{a^2\sin^2\nu + b^2\cos^2\nu}\ ,$$

$$M = 0\,,$$

$$N = ab/\sqrt{a^2\sin^2\nu + b^2\cos^2\nu}\ ,$$

$$E = a^2\cos^2\nu\ ,$$

$$F = 0\,, \text{ and}$$

$$G = a^2\sin^2\nu + b^2\cos^2\nu\ .$$

The two principal curvatures on the surface are, then, given by

$$\kappa_1 = L/E = \frac{b}{a\sqrt{a^2\sin^2\nu + b^2\cos^2\nu}} \tag{45}$$

and

$$\kappa_2 = N/G = \frac{ab}{\sqrt{(a^2\sin^2\nu + b^2\cos^2\nu)^{3/2}}} \tag{46}$$

which can, also, be expressed as

$$\kappa_1 = \frac{c}{a}\sqrt{\frac{a^2\cos^2\theta + b^2\sin^2\theta}{a^4\cos^2\theta + b^4\sin^2\theta}} \tag{47}$$

and

$$\kappa_2 = \frac{ab(a^2\cos^2\theta + b^2\sin^2\theta)^{3/2}}{(a^4\cos^2\theta + b^4\sin^2\theta)^{3/2}} \quad . \tag{48}$$

It is noticed that $R_1 = \frac{1}{\kappa_1}$ and $R_2 = \frac{1}{\kappa_2}$ as found in Table 1. Since F=M=0, the directions $\vec{R}_\phi$ and $\vec{R}_\nu$ are in the principal surface directions [3] which are expressed by τ_1, $\hat{\tau}_2$ and are associated with κ_1 and κ_2, respectively, as shown in Figure 7. If β denotes the angle between $\hat{t}$ and $\hat{\tau}_1$, then

$$\hat{t} = \hat{\tau}_1\cos\beta + \hat{\tau}_2\sin\beta \quad . \tag{49}$$

From Euler's theorem, the normal curvature along the geodesic path is specified by

$$\kappa_g = \kappa_1\cos^2\beta + \kappa_2\sin^2\beta \tag{50}$$

with the radius of curvature (ρ_g) being $1/\kappa_g$.

The torsion term (T_o) introduced in Section II(B) is given by

$$T_o = T \rho_g$$

where the surface torsion is given by

$$T = \frac{\sin 2\beta}{2} (\kappa_2 - \kappa_1) \tag{52}$$

with κ_1 and κ_2 being defined in Equaitons (45)-(48).

C. Surface Geodesics

The geodesics on the cylinder, cone and spheroid are examined in this section.

(a) Cylinder case:

The circular cylinder geometry used for this study is shown in Figure 8(a). Since the cylinder is a developed surface, the geodesic path Q'Q is a straight line on the unfolded planar surface. As shown in Figure 8(b), the geodesic unit tangent $\hat{t}$ is given by

$$\hat{t} = \hat{\phi} \cos\gamma + \hat{z} \sin\gamma \tag{53}$$

where

$$\hat{\phi} = -\sin\phi \hat{x} + \cos\phi \hat{y}. \tag{54}$$

It is noticed that $\hat{\phi}$ and $\hat{z}$ are the two principal directions on the cylinder surface. For a given geodesic Q'Q, one can see that γ is a constant along the geodesic path.

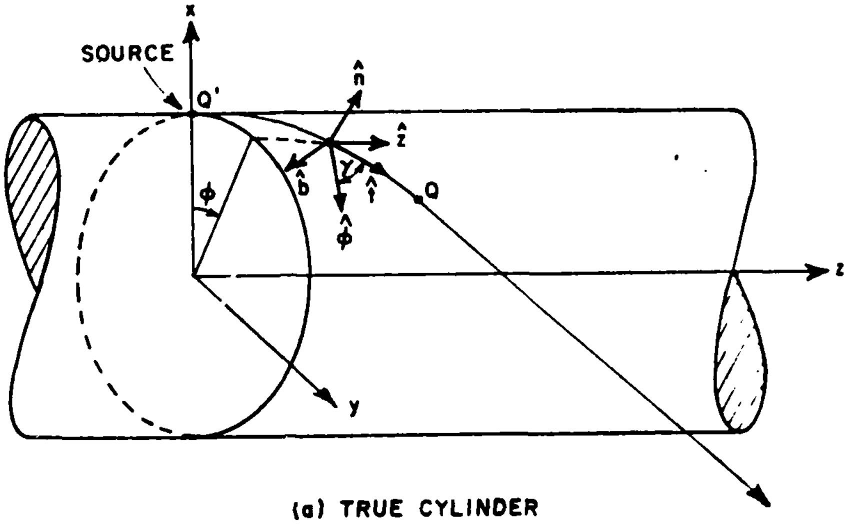

(a) TRUE CYLINDER

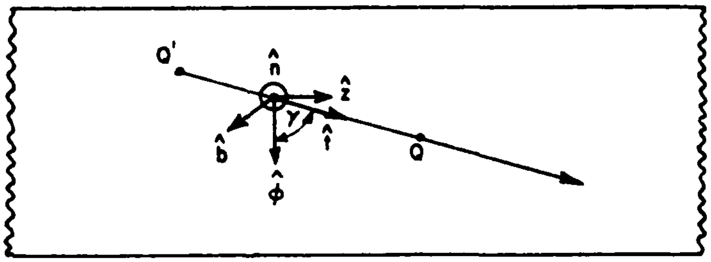

(b) UNFOLDED PLANAR SURFACE

Figure 8. Geodesic path on a developed cylinder.

(b) Cone case:

Consider a ray propagates along a geodesic path Q'Q on the cone surface as shown in Figure 9(a) which is a straight line on the unfolded planar surface as shown in Figure 9(b) since the cone is a developed surface. Applying the same technique as in Section B, $\hat{t}_e$ and $\hat{\phi}$ are the two principal directions on the surface. The geodesic unit tangent $\hat{t}$ is, then, represented by

$$\hat{t} = \hat{\phi}\cos\beta + \hat{t}_e\sin\beta \tag{55}$$

where

$$\hat{t}_e = -\hat{x}_e\sin\delta + \hat{z}\cos\delta \;, \tag{56}$$

$$\hat{x}_e = \cos\phi\hat{x} + \sin\phi\hat{y}, \tag{57}$$

and δ is the half cone angle as shown in Figure 9(a). Note that β is no longer a constant along the geodesic path Q'Q.

(c) Spheroid case:

Recall that the prolate spheroid surface is defined by

$$\vec{R}(\nu,\phi) = a\cos\nu\cos\phi\hat{x} + a\cos\nu\sin\phi\hat{y} + b\sin\nu\hat{z}$$

with

$$\tan\nu = \frac{b\cos\theta}{a\sin\phi}\;.$$

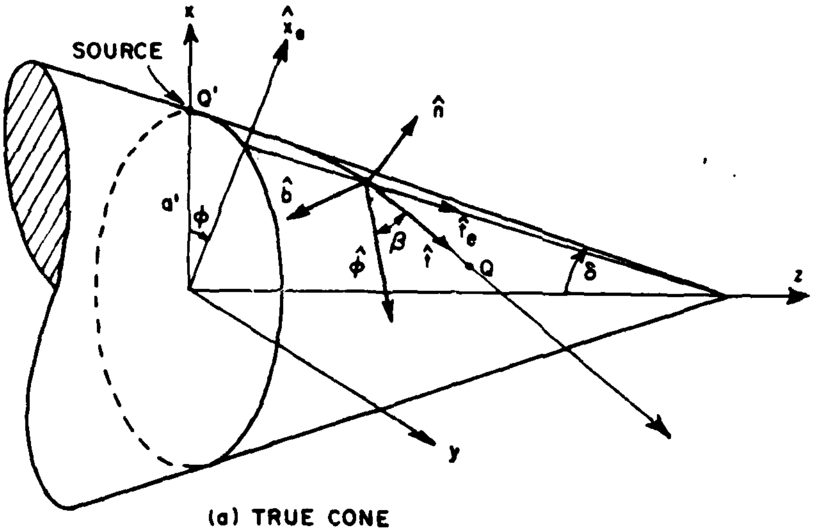

(a) TRUE CONE

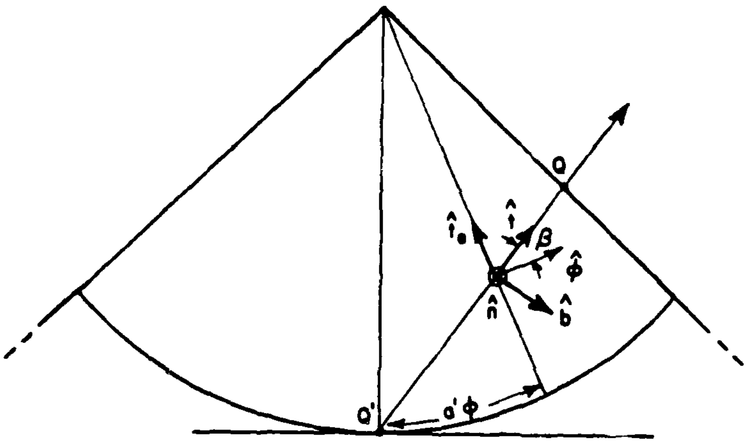

(b) UNFOLDED PLANAR SURFACE

Figure 9. Geodesic path on a developed cone.

From Section B, it was found that the principal directions were given by $\vec{R}_\phi$ and $\vec{R}_\nu$. As seen in Figure 10(a) and (b) the unit vectors in the principal directions can be represented by

$$\hat{t}_r = \vec{R}_\phi / |\vec{R}_\phi| = -\hat{x}\sin\phi + \hat{y}\cos\phi \tag{58}$$

$$\hat{t}_e = \vec{R}_\nu / |\vec{R}_\nu| = -\hat{x}_e \sin\delta + \hat{z}\cos\delta$$

$$= \frac{-a\ \sin\nu\hat{x}_e + b\ \cos\nu\hat{z}}{\sqrt{a^2\sin^2\nu + b^2\cos^2\nu}} \tag{59}$$

with

$$\hat{x}_e = \cos\phi\hat{x} + \sin\phi\hat{y}\ . \tag{60}$$

It is noticed that $\hat{t}_r$ is merely $\hat{\phi}$. If β denotes the angle between $\hat{t}_r$ and the geodesic unit tangent $\hat{t}$, then

$$\hat{t} = \hat{t}_r\cos\beta + \hat{t}_e\sin\beta\ , \tag{61}$$

which is identical to the form used for the cylinder and cone geodesics. This suggests that one might be able to develop a perturbation solution which gives a simplified form for β on a spheroid using the cylinder or cone expressions for β.

D. Cylinder Perturbation for Near Field

In order to solve for the geodesic paths on a prolate spheroid for the near zone, the cylinder perturbation technique is used when the source is located at or near $\theta_s = 90^0$. As shown in Figure 11, the cylinder is perturbed by bending it around the spheroid, and the geodesic paths are to be resolved in this perturbed cylinder model.

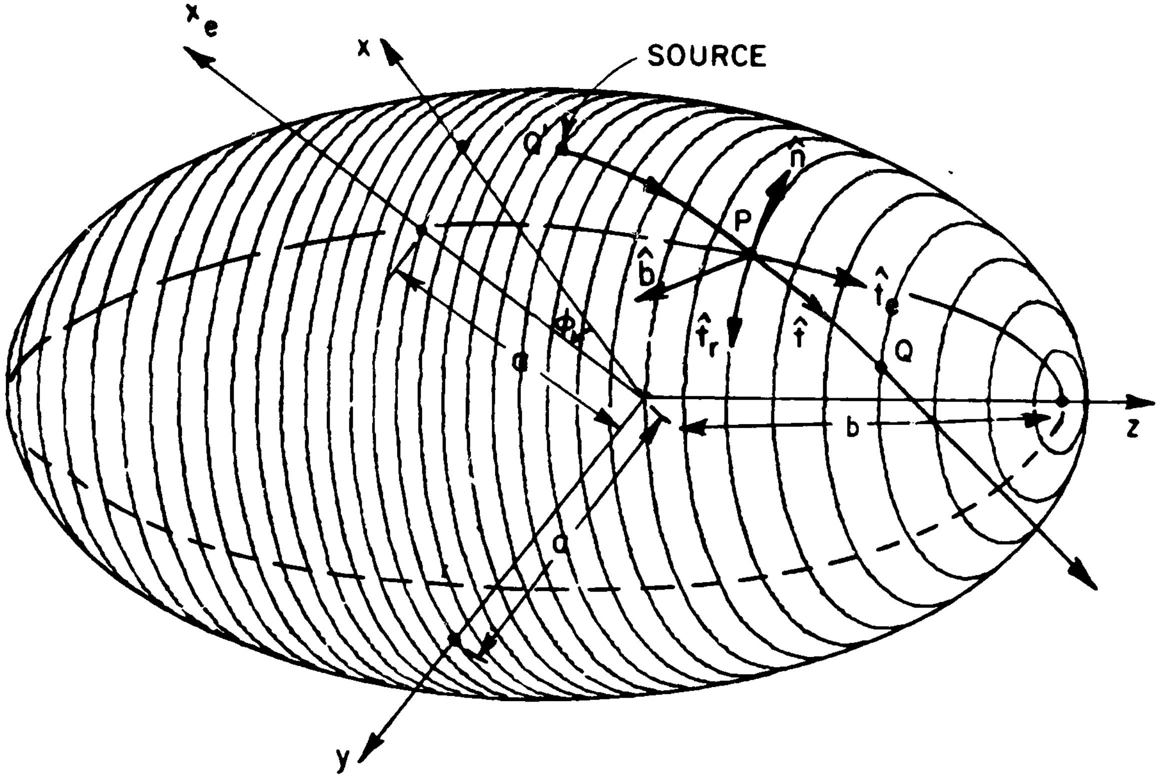

Figure 10(a). Geodesic path on a spheroid.

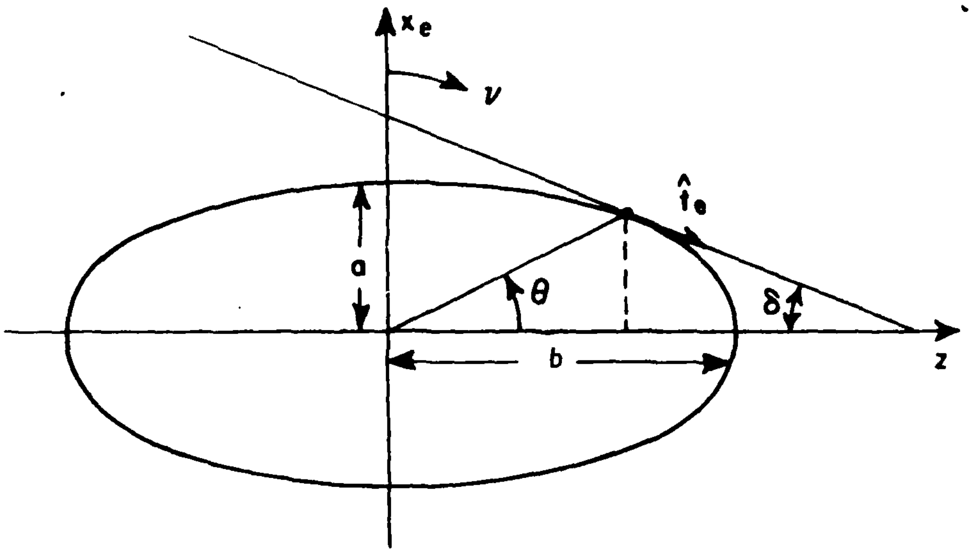

Figure 10(b). Elliptic profile.

Recalling that γ is a constant along a given geodesic path Q'Q on the perturbed cylinder in Figure 11, one obtains a geodesic equation given by

$$\tan\gamma = \frac{S_e}{S_r} \tag{62}$$

with $S_r = a\phi_r$, where ϕ_r is measured from the source to the diffraction point. The elliptic cross-section in the x_e-z plane is described by

$x_e = a \cos\nu_e$ and

$z = b \sin\nu_e$

therefore, the arclength is given by

$$S_e = \int_0^{\nu_e} \sqrt{a^2\sin^2\nu + b^2\cos^2\nu}\, d\nu$$

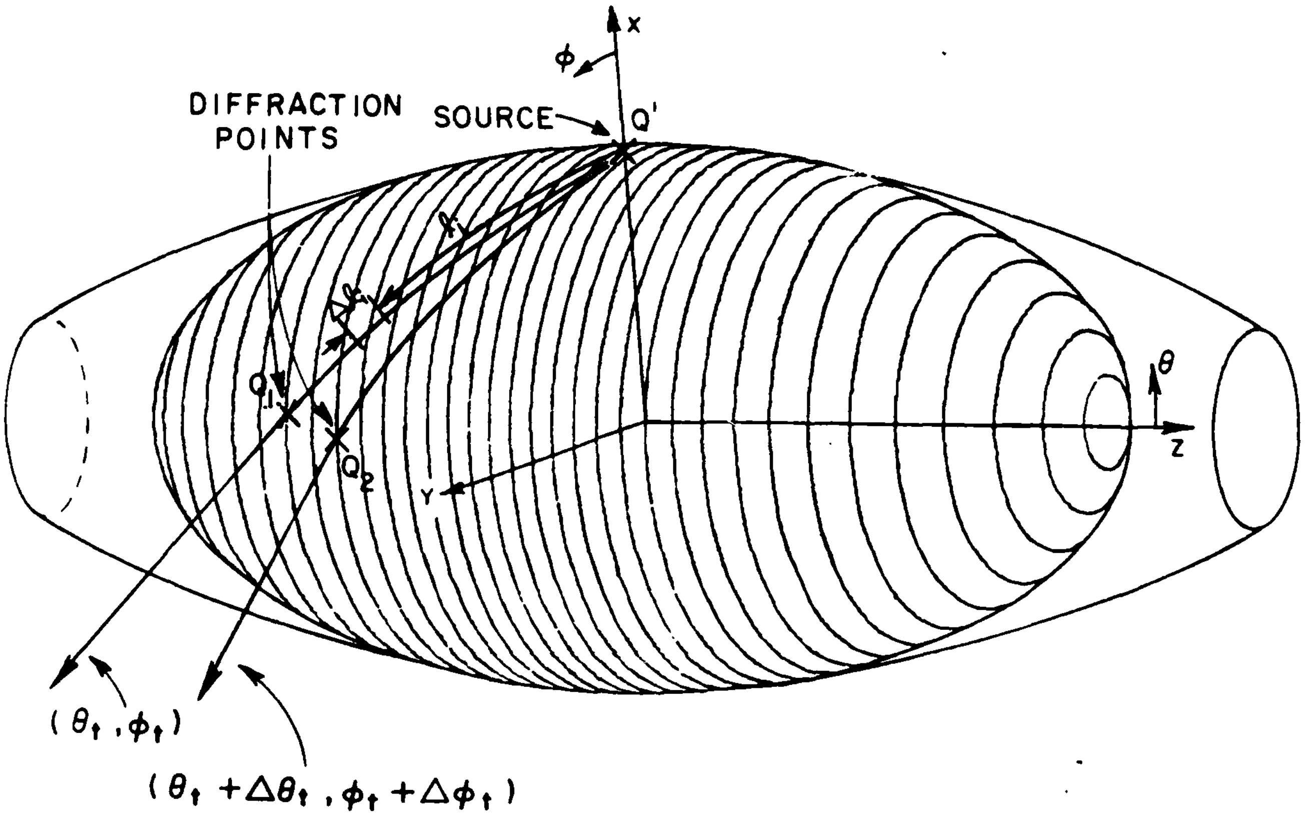

Figure 11. Cylinder perturbation.

Thus, Equation (62) becomes

$$\tan\gamma = \frac{\int_{0}^{\nu_e} \sqrt{a^2\sin^2\nu + b^2\cos^2\nu}\, d\nu}{a\phi_r} \tag{63}$$

with $-\pi \leq \gamma \leq \pi$, $-\pi/2 \leq \phi_r, \nu_e \leq \pi/2$.

Assuming the diffraction point Q $(a\cos\nu_e\cos\phi_r,\ a\cos\nu_e\sin\phi_r,\ b\sin\nu_e)$ and the receiver point P_s $(R_t\sin\theta_t\cos\phi_t,\ R_t\sin\theta_t\sin\phi_t,\ R_t\cos\theta_t)$, then at the diffraction point Q, the radiation direction (θ_t, ϕ_t) should coincide with the geodesic tangent $\hat{t}$ given in Equation (61). Thus,

$$\begin{aligned} \hat{t} &= \hat{x}\, t_x + \hat{y}\, t_y + \hat{z}\, t_z \\ &= \hat{t}_r \cos\gamma + \hat{t}_e \sin\gamma \end{aligned} \tag{64}$$

where,

$$t_x = \frac{R_t\sin\theta_t\cos\phi_t - a\cos\nu_e\cos\phi_r}{D},$$

$$t_y = \frac{R_t\sin\theta_t\sin\phi_t - a\cos\nu_e\sin\phi_r}{D},$$

$$t_z = \frac{R_t\cos\theta_t - b\sin\nu_e}{D}, \text{ and}$$

$$\begin{aligned} D^2 = {} & R_t^2 - 2R_t[a\sin\theta_t\cos\nu_e\cos(\phi_t - \phi_r) + b\cos\theta_t\sin\nu_e] \\ & + a^2\cos^2\nu_e + b^2\sin^2\nu_e \quad . \end{aligned}$$

Equating the x-, y-, and z-components respectively, one obtains

$$-\sin\phi_r\cos\gamma - \frac{a\ \sin\nu_e\cos\phi_r\sin\ \gamma}{\sqrt{a^2\sin^2\nu_e + b^2\cos^2\ \nu_e}} = \frac{R_t\sin\theta_t\cos\phi_t - a\ \cos\nu_e\cos\phi_r}{D} \tag{65}$$

$$\cos\phi_r\cos\gamma - \frac{a\ \sin\nu_e\sin\phi_r\sin\gamma}{\sqrt{a^2\sin^2\nu_e + b^2\cos^2\nu_e}} = \frac{R_t\sin\theta_t\sin\phi_t - a\ \cos\nu_e\sin\phi_r}{D} \tag{66}$$

$$\frac{b\ \cos\nu_e\sin\ \gamma}{\sqrt{a^2\sin^2\nu_e+b^2\cos^2\nu_e}} = \frac{R_t\ \cos\theta_t - b\ \sin\nu_e}{D} \tag{67}$$

From equations (65) and (66), one obtains

$$\cos\ \gamma = \frac{R_t\sin\theta_t\sin(\phi_t-\phi_r)}{D} \tag{68}$$

and

$$-\frac{a\ \sin\nu_e\sin\gamma}{\sqrt{a^2\sin^2\nu_e+b^2\cos^2\nu_e}} = \frac{R_t\sin\theta_t\cos(\phi_t-\phi_r)-a\ \cos\nu_e}{D}\ . \tag{69}$$

Equation (69) is divided by (67) to give

$$\frac{-a\ \sin\nu_e}{b\ \cos\nu_e} = \frac{R_t\sin\theta_t\cos(\phi_t-\phi_r)}{R_t\cos\theta_t-b\ \sin\nu_e}\ . \tag{70}$$

From Equations (62), (67) and (68), one obtains

$$\frac{b\cos\nu_e S_e}{a\phi_r\sqrt{a^2\sin^2\nu_e+b^2\cos^2\nu_e}} = \frac{R_t\cos\theta_t-b\sin\nu_e}{R_t\sin\theta_t\sin(\phi_t-\phi_r)} \tag{71}$$

From Equations (70) and (71), one obtains

$$f(R_t,\theta_t,\phi_r,\nu_e,\phi_r) = b\sin\theta_t\cos(\phi_t-\phi_r)\cos\nu_e+a\cos\theta_t\sin\nu_e - \frac{ab}{R_t} = 0 \text{ , and} \tag{72}$$

$$g(R_t,\theta_t,\phi_t,\nu_e,\phi_r) = b\,S_e\sin\theta_t\sin(\phi_t-\phi_r)\cos\nu_e-a\phi_r\sqrt{a^2\sin^2\nu_e+b^2\cos^2\nu_e}\cos\theta_t + \frac{ab\phi_r\sqrt{a^2\sin^2\nu_e+b^2\cos^2\nu_e}\sin\nu_e}{R_t} = 0 \tag{73}$$

Provided that one has obtained a diffraction point (ν_e,ϕ_r) for a receiver location (R_t,θ_t,ϕ_t), a numerical technique can now be developed from Equations (72) and (73) to solve for $(\nu_e+\Delta\nu_e,\ \phi_r+\Delta\phi_r)$ associated with a new receiver location $(R_t+\Delta R_t,\ \theta_t+\Delta\theta_t,\phi_t+\Delta\phi_t)$. Assuming that the ith set of $(\theta_t,\phi_t,\nu_e,\phi_e)$ is first known to satisfy $f_i=g_i=0$, or at least approximately so, the next set $(R_t+\Delta R_t,\theta_t+\Delta\theta_t,\phi_t+\Delta\phi_t,\nu_e+\Delta\nu_e,\phi_r+\Delta\phi_r)$ is obtained by enforcing $f_{i+1}=g_{i+1}=0$, such that

$$f_{i+1} = f_i+f_{R_t}\Delta R_t + f_{\theta_t}\Delta\theta_t+f_{\phi_t}\Delta\theta_t + f_{\nu_e}\Delta\nu_e + f_{\phi_r}\Delta\phi_r = 0, \text{ and}$$

$$g_{i+1} = g_i+g_{R_t}\Delta R_t + g_{\theta_t}\Delta\theta_t + g_{\phi_t}\Delta\phi_t + g_{\nu_e}\Delta\nu_e + g_{\phi_r}\Delta\phi_r = 0$$

In matrix form, it is given by

$$\begin{bmatrix} f_{\nu_e} & f_{\phi_r} \\ g_{\nu_e} & g_{\phi_r} \end{bmatrix} \begin{bmatrix} \Delta\nu_e \\ \Delta\phi_r \end{bmatrix} = \begin{bmatrix} -f_i - f_{R_t}\,\Delta R_t - f_{\theta_t}\Delta\theta_t - f_{\phi_t}\Delta\phi_t \\ -g_i - g_{R_t}\,\Delta R_t - g_{\theta_t}\Delta\theta_t - g_{\phi_t}\Delta\phi_t \end{bmatrix} \tag{74}$$

$$f_{\nu_e} = -b\,\sin\theta_t\cos(\phi_t-\phi_r)\sin\nu_e + a\,\cos\theta_t\cos\nu_e$$

$$f_{\phi_r} = b\,\sin\theta_t\cos\nu_e\sin(\phi_t-\phi_r)$$

$$f_{R_t} = \frac{ab}{R_t^2}$$

$$f_{\theta_t} = b\,\cos\theta_t\cos(\phi_t-\phi_r)\cos\nu_e - a\,\sin\theta_t\sin\nu_e$$

$$f_{\phi_t} = -b\,\sin\theta_t\sin(\phi_t-\phi_r)\cos\nu_e$$

$$g_{\nu_e} = b\quad\sin\theta_t\sin(\phi_t-\phi_r)\left[D_{Se}\cos\nu_e - S_e\sin\nu_e\right] - a\phi_r\,D'_{Se}\cos\theta_t + \frac{ab\phi_r}{R_t}\left[D'_{Se}\sin\nu_e + D_{Se}\,\cos\nu_e\right]$$

$$g_{\phi_r} = -b\,S_e\,\sin\theta_t\cos(\phi_t-\phi_r)\cos\nu_e - a\,D_{Se}\cos\theta_t + \frac{ab}{R_t}D_{Se}\,\sin\nu_e$$

$$g_{R_t} = -\,\frac{ab\phi_r D_{Se}\sin\nu_e}{R_t^2}$$

$$g_{\theta_t} = b\,S_e\,\cos\theta_t\sin(\phi_t-\phi_r)\cos\nu_e + a\phi_r D_{Se}\sin\theta_t$$

$$G_{\phi_t} = b\,S_e\,\sin\theta_t\cos(\phi_t-\phi_r)\cos\nu_e$$

$$D_{Se} = \sqrt{a^2 \sin^2 \nu_e + b^2 \cos^2 \nu_e}$$

$$D'_{Se} = \frac{(a^2-b^2)\cos\nu_e \sin\nu_e}{\sqrt{a^2\sin^2\nu_e + b^2\cos^2\nu_e}}$$

Therefore, one obtains $(\Delta\nu_e, \Delta\phi_r)$ for a known $(\Delta R_t, \Delta\theta_t, \Delta\phi_t)$ using Equation (74). In order to determine the initial diffraction point (ν_e, ϕ_r) for a receiver location (R_t, θ_t, ϕ_t), one can always assume a diffraction point at the source $(\nu_s, \phi_s) = (0,0)$ with the radiation direction $(\theta_t, \pi/2)$ for the positive ray (in +y direction) or $(\theta_t, 3\pi/2)$ for the negative ray (in $-\hat{y}$ direction), and gradually add increments $(\Delta R_t, \Delta\theta_t, \Delta\phi_t)$ until the desired receiver location (R_t, θ_t, ϕ_t) is reached. After the initial diffraction point is identified by (ν_e, ϕ_r); γ, and therefore, the geodesic path is determined by Equation (63). Such a numerical approach is illustrated in Figure 9. Note that one need not trace out the complete geodesic path from the source location to the diffraction point for each new radiation direction. As shown in Figure 9, the diffraction point $(\nu_e + \Delta\nu_e, \phi_r + \Delta\phi_r)$ for the next receiver location is determined from (ν_e, ϕ_r), using Equation (74), if $(\Delta R_t, \Delta\theta_t, \Delta\phi_t)$ are small which is the case when a complete radiation pattern is computed.

After the geodesic path is determined, various other parameters associated with Equations (15)-(18) must be found. The Fock parameter of Equation (12) is given by

$$\xi = \int_{Q'}^{Q} \frac{1}{\rho_g} \left(\frac{k\rho_g}{2} \right)^{1/3} d\ell ,$$

where the integral is evaluated along the geodesic path. Note that ℓ is the arc length along the geodesic and given by

$$\ell = \frac{S_e}{\sin\gamma} = \frac{S_r}{\cos\gamma} \ .$$

Therefore,

$$d\ell = \frac{1}{\sin\gamma}\sqrt{a^2\sin^2\nu+b^2\cos^2\nu d\nu}$$

or,

$$d\ell = \frac{1}{\cos\gamma} \ a d\phi ,$$

and the integration can be rewritten as

$$\xi = \frac{1}{\sin\gamma}\int_0^{\nu_e} \frac{1}{\rho_g}\left(\frac{k\rho_g}{2}\right)^{1/3} \sqrt{a^2\sin^2\nu'+b^2\cos^2\nu'}d\nu' \tag{75}$$

or

$$\xi = \frac{a}{\cos\gamma}\int_0^{\phi_r} \frac{1}{\rho_g}\left(\frac{k\rho_g}{2}\right)^{1/3} d\phi' \ . \tag{76}$$

where $\rho_g = 1/(\kappa_1\cos^2\gamma+\kappa_2\sin^2\gamma)$, and κ_1, κ_2 are given in Equations (45) and (46).

Next, the ray divergence factor $\sqrt{\frac{d\psi_0(Q')}{d\psi(Q)}}$ is defined as the change in the separation of adjacent surface rays as shown in Figure 12. It is assumed since the prolate spheroid will be long and slender that the ray divergence factor is unity. Note that it is unity for a cylinder.

E. Cone Perturbation for Near Field

When the source is not located at the mid-section ($\theta_s \neq 90^0$, in Figure 14), the cone perturbation model is used. As shown in Figure 13(a),

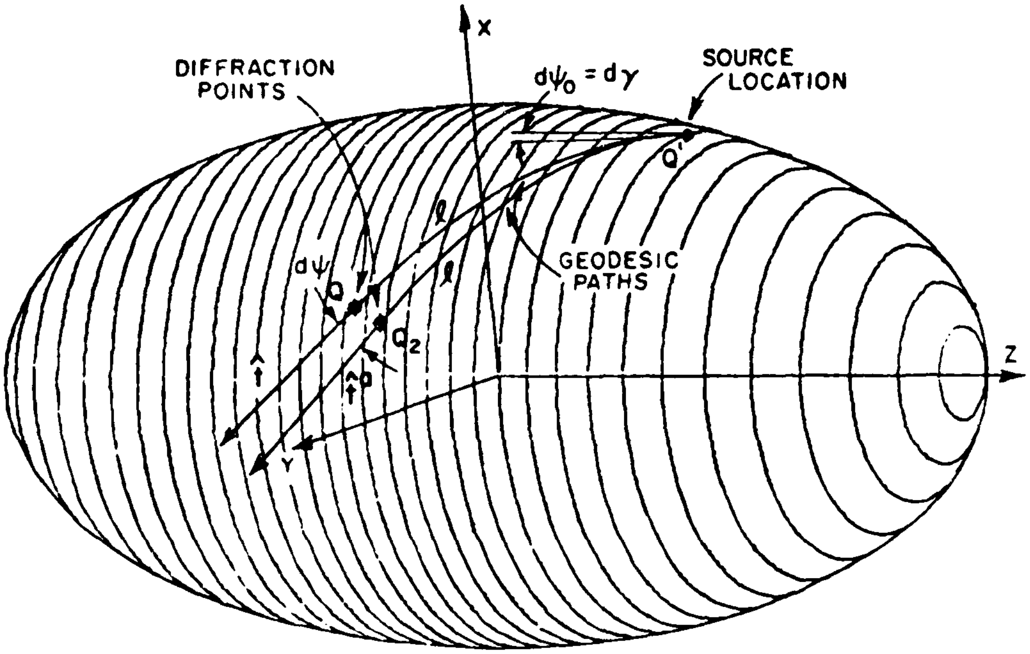

Figure 12. Illustration of the spread factor ($\sqrt{d\psi_0/d\psi}$) terms.

the spheroid is modeled by a perturbed cone. The associated unfolded surface is shown in Figure 13(b). If γ and β denote the angle between t and $\hat{t}_r$ at Q' and Q, respectively, it is seen in Section III-(B) that they are not the same as in the cylinder case. In fact,

$$\beta = \gamma - \alpha \tag{79}$$

where

$$\alpha = \frac{S_r}{r} = \frac{a'\phi}{r}$$

with $a' = a\cos\nu_x$ and $\tan\nu_s = \dfrac{a\cos\theta_s}{b\sin\theta_s}$. With some manipulation, one can show that

$$(r - S_e)\cos(\gamma - \alpha) = r\cos\gamma \tag{80}$$

where

$$S_e = \int_{\nu_s}^{\nu_e} \sqrt{a^2\sin^2\nu_e' + b^2\cos^2\nu_e'}\, d\nu_e'.$$

The line going from the diffraction point Q $(a\cos\nu_e\cos\phi_r, a\cos\nu_e\sin\phi_r, b\sin\nu_e)$ to the receiver location (R_t, θ_t, ϕ_t) coincides with the geodesic tangent $\hat{t}$, and one obtains

$$-\sin\phi_r\cos(\gamma-\alpha) - \frac{a\sin\nu_e\cos\phi_r}{\sqrt{a^2\sin^2\nu_e + b^2\cos^2\nu_e}}\sin(\gamma-\alpha) = \frac{R_t\sin\theta_t\cos\phi_t - a\cos\nu_e\cos\phi_r}{D} \tag{81}$$

$$\cos\phi_r\cos(\gamma-\alpha) - \frac{a\sin\nu_e\sin\phi_r}{\sqrt{a^2\sin^2\nu_e + b^2\cos^2\nu_e}}\sin(\gamma-\alpha) = \frac{R_t\sin\theta_t\sin\phi_t - a\cos\nu_e\sin\phi_r}{D} \tag{82}$$

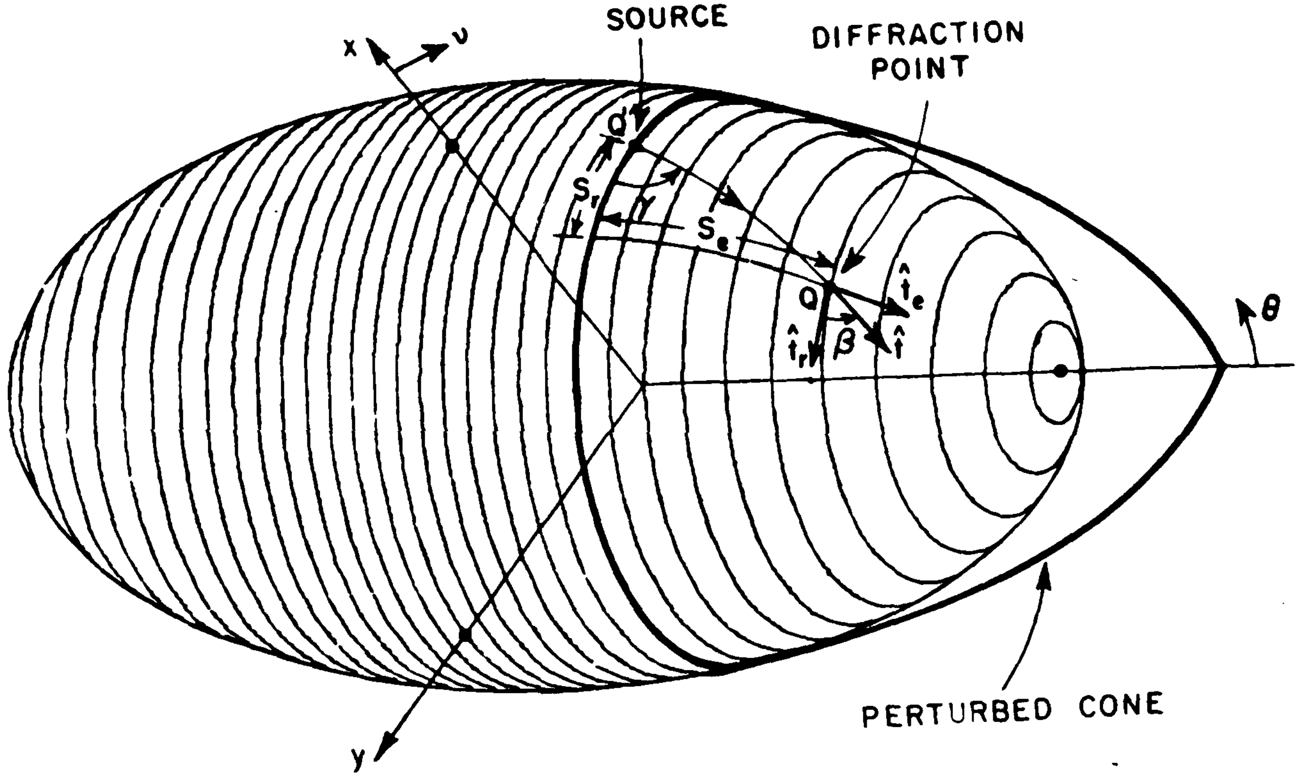

Figure 13(a). Geodesic path on the perturbed cone.

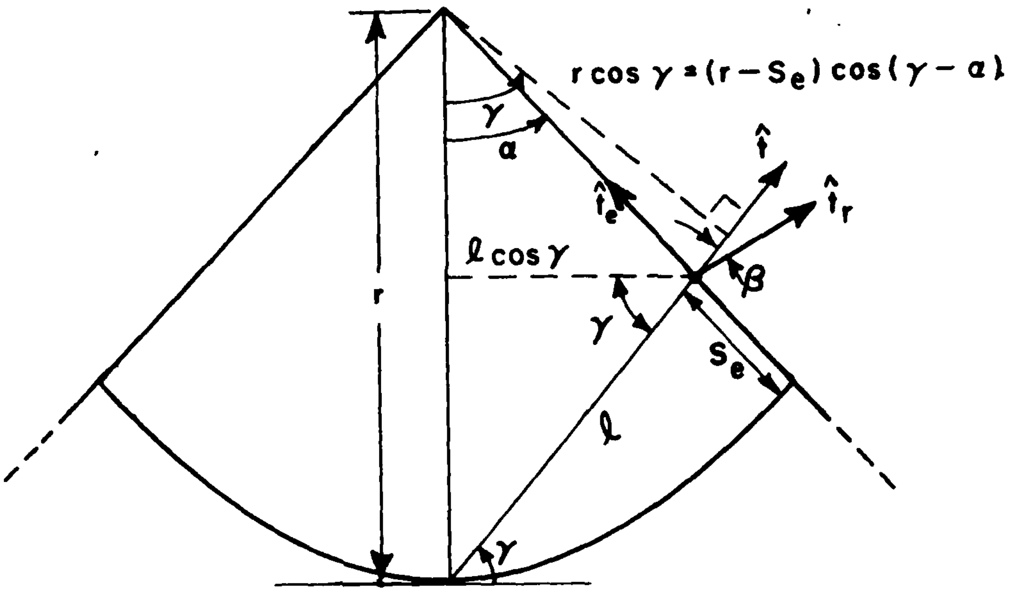

Figure 13(b). Geodesic path on the unfolded cone.

$$\frac{b\cos\nu_e\sin(\gamma-\alpha)}{\sqrt{a^2\sin^2\nu_e+b^2\cos^2\nu_e}} = \frac{R_t\cos\theta_t-b\sin\nu_e}{D}\ . \tag{83}$$

From Equations (81) and (82), one obtains

$$\cos(\gamma-\alpha) = \frac{R_t\sin\theta_t\sin(\phi_t-\phi_r)}{D}\ , \tag{84}$$

and

$$-\frac{a\sin\nu_e\sin(\gamma-\alpha)}{\sqrt{a^2\sin^2\nu_e+b^2\cos^2\nu_e}} = \frac{R_t\sin\theta_t\cos(\phi_t-\phi_r)-a\cos\nu_e}{D} \tag{85}$$

Equation (85) is divided by (83) to give

$$-\frac{a\sin\nu_e}{b\cos\nu_e} = \frac{R_t\sin\theta_t\cos(\phi_t-\phi_r)-a\cos\nu_e}{R_t\cos\theta_t - b\sin\nu_e}\ . \tag{86}$$

Therefore, one obtains

$$f(\nu_e,\gamma,\alpha) = (r-S_e)\cos(\gamma-\alpha)-r\cos\gamma = 0 \tag{87}$$

$$g(\theta_t,\phi_t,\nu_e\gamma,\alpha) = D'\cos(\gamma-\alpha)-\sin\theta_t\sin(\phi_t - \frac{r}{a'}\alpha) = 0 \tag{88}$$

$$\begin{aligned} h(\theta_t,\phi_t,\nu_e,\alpha) = {} & a\sin\nu_e\cos\theta_t+b\sin\theta_t\cos\nu_e\cos(\phi_t - \frac{r\alpha}{a'}) \\ & - \frac{ab}{R_t} = 0 \end{aligned} \tag{89}$$

where

$$\begin{aligned} D' = \Bigg\{ & 1-2\left[\frac{a}{R_t}\sin\theta_t\cos\nu_e\cos(\phi_t - \frac{r\alpha}{a'})+\frac{b}{R_t}\cos\theta_t\sin\nu_e\right] \\ & + \frac{a^2}{R_t^2}\cos^2\nu_e + \frac{b^2}{R_t^2}\sin^2\nu_e\Bigg\}^{1/2} . \end{aligned}$$

Using the increment method again, one uses

$$f_{i+1} = f_i + f_{\nu_e}\Delta\nu_e + f_\alpha\Delta\alpha + f_\gamma\Delta\gamma = 0$$

$$g_{i+1} = g_i + g_{\nu_e}\Delta\nu_e + g_\alpha\Delta\alpha + g_\gamma\Delta\gamma + g_{\theta_t}\Delta\theta_t + g_{\phi_t}\Delta\phi_t + g_{R_t}\Delta R_t = 0$$

$$h_{i+1} = h_i + h_{\nu_e}\Delta\nu_e + h_\alpha\Delta\alpha + h_{\theta_t}\Delta\theta_t + h_{\phi_t}\Delta\phi_t + h_{R_t}\Delta R_t = 0$$

In matrix form, it is given by

$$\begin{bmatrix} f_{\nu_e} & f_\alpha & f_\gamma \\ g_{\nu_e} & g_\alpha & g_\gamma \\ h_{\nu_e} & h_\alpha & 0 \end{bmatrix} \begin{bmatrix} \Delta\nu_e \\ \Delta\alpha \\ \Delta\gamma \end{bmatrix} = \begin{bmatrix} -f_i \\ -g_i - g_{\theta_t}\Delta\theta_t - g_{\phi_t}\Delta\phi_t - g_{R_t}\Delta R_t \\ -h_i - h_{\theta_t}\Delta\theta_t - h_{\phi_t}\Delta\phi_t - h_{R_t}\Delta R_t \end{bmatrix} \tag{90}$$

$$f_{\nu_e} = -\sqrt{a^2\sin^2\nu_e + b^2\cos^2\nu_e}\,\cos(\gamma-\alpha)$$

$$f_\alpha = (r-S_e)\sin(\gamma-\alpha)$$

$$f_\gamma = r\sin\gamma - (r-S_e)\sin(\gamma-\alpha)$$

$$g_{\nu_e} = \frac{\cos(\gamma-\alpha)}{D'}\left[\frac{(b^2-a^2)}{R_t^2}\sin\nu_e\cos\nu_e + \frac{a}{R_t}\sin\nu_e\sin\theta_t\cos\left(\phi_t - \frac{r\alpha}{a'}\right) - \frac{b}{R_t}\cos\nu_e\cos\theta_t\right]$$

$$g_\alpha = D'\sin(\gamma-\alpha) + \sin\theta_t\cos\left(\phi_t - \frac{r}{a'}\alpha\right)\frac{r}{a'} + \frac{\cos(\gamma-\alpha)}{D'}\left[-\frac{a}{R_t}\cos\nu_e\sin\theta_t\sin\left(\phi_t - \frac{r\alpha}{a'}\right)\frac{r}{a'}\right]$$

$$g_\gamma = -D'\sin(\gamma-\alpha)$$

$$g_{\theta_t} = -\cos\theta_t \sin\left(\phi_t - \frac{r}{a'}\alpha\right) + \frac{\cos(\gamma-\alpha)}{D'}\left[\frac{b}{R_t}\sin\theta_t\sin\nu_e - \right.$$

$$\left.\frac{a}{R_t}\cos\theta_t\cos\nu_e\cos\left(\phi_t - \frac{r}{a'}\alpha\right)\right]$$

$$g_{\phi_t} = -\sin\theta_t\cos\left(\phi_t - \frac{r}{a'}\alpha\right) + \frac{\cos(\gamma-\alpha)}{D'}\left[\frac{a}{R_t}\sin\theta_t \cos\nu_e\sin\left(\phi_t - \frac{r}{a'}\alpha\right)\right]$$

$$g_{R_t} = \frac{\cos(\gamma-\alpha)}{D'R_t}\left\{\left[\frac{a}{R_t}\sin\theta_t\cos\nu_e\cos\left(\phi_t - \frac{r\alpha}{a'}\right) + \frac{b}{R_t}\cos\theta_t\sin\nu_e\right]\right.$$

$$\left. - \frac{a^2}{R_t^2}\cos^2\nu_e - \frac{b^2}{R_t^2}\sin^2\nu_e\right\}$$

$$h_{\nu_e} = a\cos\nu_e\cos\theta_t - b\sin\nu_e\sin\theta_t\cos\left(\phi_t - \frac{r}{a'}\alpha\right)$$

$$h_\alpha = b\cos\nu_e\sin\theta_t\sin\left(\phi_t - \frac{r}{a'}\alpha\right)\frac{r}{a'}$$

$$h_\gamma = 0$$

$$h_{\theta_t} = -a\sin\nu_e\sin\theta_t + b\cos\theta_t\cos\nu_e\cos\left(\phi_t - \frac{r}{a'}\alpha\right)$$

$$h_{\phi_t} = -b\sin\theta_t\cos\nu_e\sin\left(\phi_t - \frac{r}{a'}\alpha\right)$$

$$h_{R_t} = \frac{ab}{R_t^2}\ .$$

It is seen that one can solve for $(\Delta\nu_e, \Delta\alpha, \Delta\gamma)$, for a known $(\Delta R_t, \Delta\theta_t, \Delta\phi_t)$, using Equation (90). To obtain a diffraction point (ν_e, ϕ_r) for a given receiver location (R_t, θ_t, ϕ_t), one can always assume the first diffraction point is at the source $(\nu,\phi) = (\nu_s,0)$ with the radiation direction $(\theta_t=\frac{\pi}{2}, \phi_t=\frac{\pi}{2})$ for positive ray (in $\hat{y}$ direction) or $(\theta_t=\frac{\pi}{2}, \phi_t=\frac{3\pi}{2})$ for negative ray (in $-\hat{y}$ direction), and gradually add the increments $(\Delta\theta_t,\Delta\phi_t)$ until the final radiation direction (θ_t,ϕ_t) is reached. Again, one need not start out from the source everytime, but obtains the new solution directly from Equation (90), provided that the new receiver location does not deviate greatly from the previous direction.

The geodesic arc length is obtained from either of the following equations:

$$\begin{aligned} \ell\cos\gamma &= (r-S_e)\sin\alpha \quad \text{, or} \\ \ell\sin\gamma &= r-(r-S_e)\cos\alpha \quad . \end{aligned} \tag{91}$$

Therefore,

$$d\ell = \left[\cos\alpha + \frac{\sin\alpha}{\tan(\gamma-\alpha)}\right]\frac{dS_e}{d\nu_e}\,\frac{d\nu_e}{\sin\gamma} \quad \text{, or}$$

$$d\ell = \left[-\tan(\gamma-\alpha)\sin\alpha + \cos\alpha\right]\frac{r\,d\alpha}{\cos(\gamma-\alpha)}$$

and the Fock paramenter ξ is obtained by integrating along ν or α, i.e.,

$$\xi = r\int_0^{\alpha}\frac{1}{\rho_g}\left(\frac{k\rho_g}{2}\right)^{1/3}\frac{[\cos\alpha' - \tan(\gamma-\alpha')\sin\alpha']}{\cos(\gamma-\alpha')}\,d\alpha', \tag{92}$$

or

$$\xi = \int_0^{\nu_e}\frac{1}{\rho_g}\left(\frac{k\rho_g}{2}\right)^{1/3}\frac{1}{\sin\gamma}\left[\cos\alpha + \frac{\sin\alpha}{\tan(\gamma-\alpha)}\right]\sqrt{a^2\sin^2\nu' + b^2\cos^2\nu'}\;d\nu' \tag{93}$$

The ray divergence factor $\sqrt{\frac{d\psi_0(Q')}{d\psi(Q)}}$, is again assumed to be unity.

This completes the cone perturbation model used to compute the geodesic ray paths on the prolate spheroid provided the source is not mounted on the mid-section of the prolate spheroid.

IV. RESULTS

The solutions presented in the previous chapters are employed here to compute the near field radiation patterns for short monopoles or slots mounted on a $2\lambda \times 10\lambda$ prolate spheroid. To show the validity of the cylinder perturbation solution, the source is placed at $\theta_s=90^0$ as shown in Figure 14. To examine different conical pattern cuts, a cartesian coordinate system (x',y',z') originally defining the spheroid geometry in Figure 14 is now rotated into (x,y,z) as shown in Figure 15. Note that the new cartesian coordinates are found by first rotating about the z'-axis the angle ϕ_c and then about the y-axis the angle θ_c. The pattern is, then, taken in the (x,y,z) coordinate system with fixed and ϕ varied.

The calculated examples are shown in Figures 16-24. The algorithm boundaries shown in Figure 25 are used in determining whether one or two rays are used in the solution. Note that β_{12} is defined automatically by the numerical solution. This is done by determining the caustic angle in the elevation pattern (β_c) and adding a few additional degrees to that value, i.e., $\beta_{12}=\beta_c+\Delta\beta$ where $2^0 \leq \Delta\beta \leq 10^0$. One would expect to observe slight discontinuities somewhere, because various numbers of rays are included in different regions.

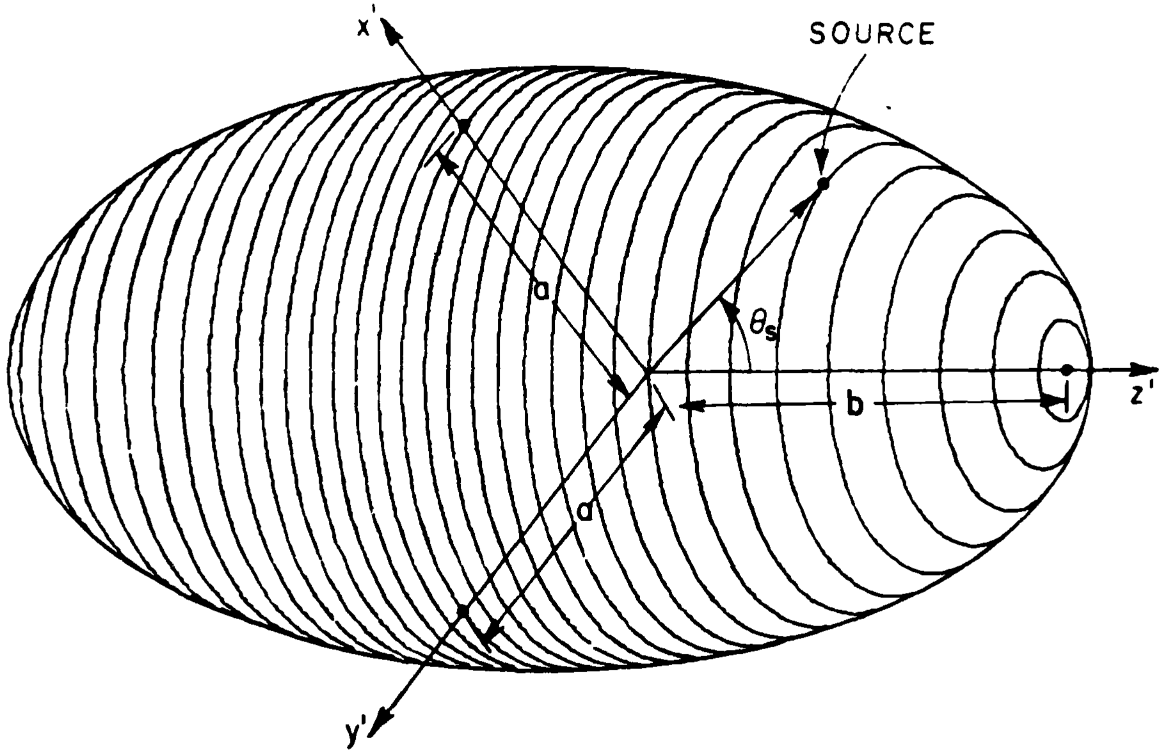

Figure 14. Geometry of a spheroid.

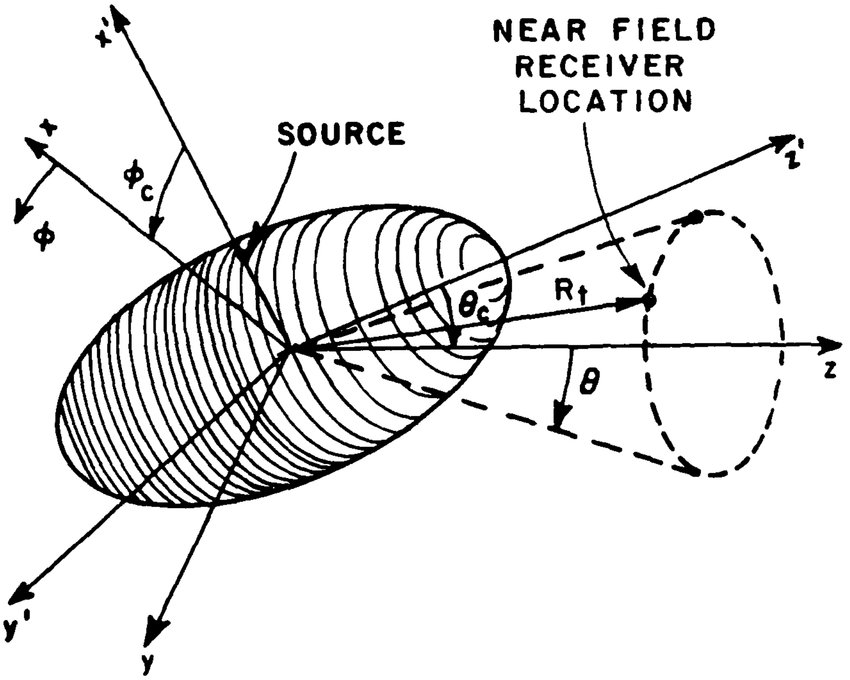

Figure 15. Definition of pattern axis.

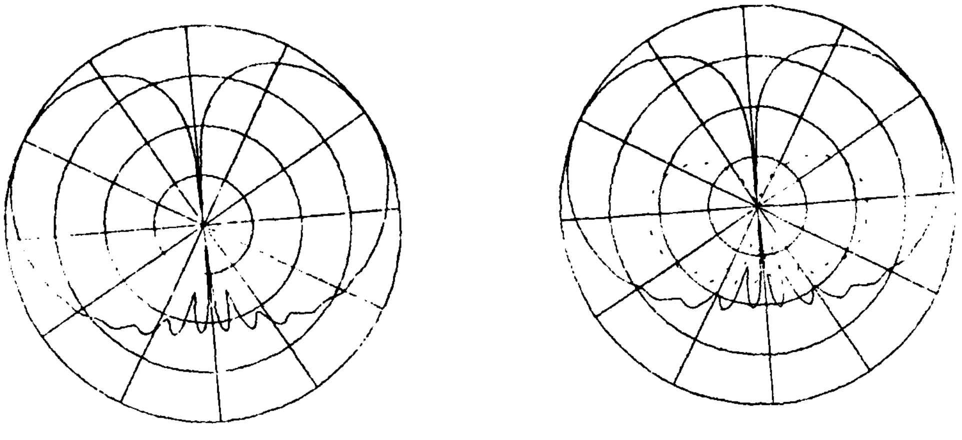

(a) $\theta_c=0^0$, $\phi_c=90^0$, $\theta=90^0$ (b) $\theta_c=30^0$, $\phi_c=90^0$, $\theta=90^0$

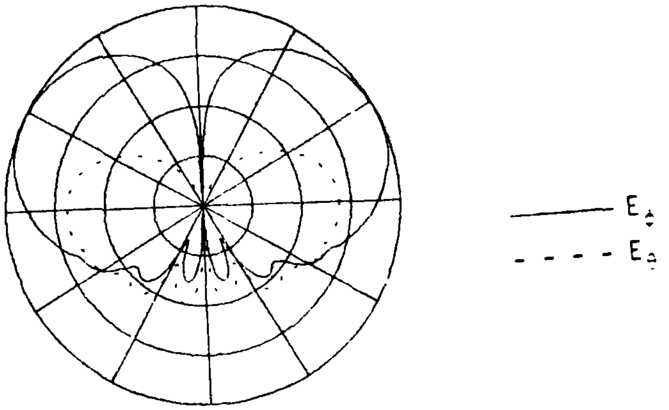

(c) $\theta_c=60^0$, $\phi_c=90^0$, $\theta=90^0$

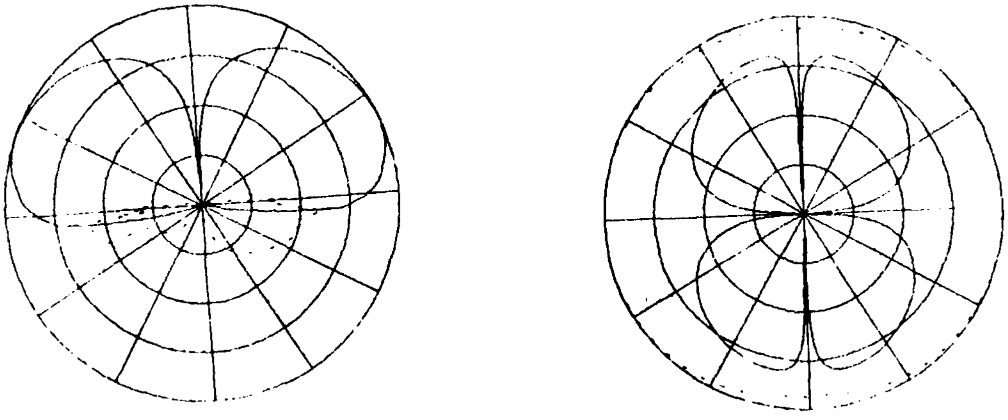

(d) $\theta_c=90^0$, $\phi_c=90^0$, $\theta=90^0$ (e) $\theta_c=90^0$, $\phi_c=0^0$, $\theta=90^0$

Figure 16. Near zone radiation patterns for $R_t=15\lambda$ for a short monopole mounted at $\theta_s=90^0$ on a $2\lambda \times 10\lambda$ spheroid.

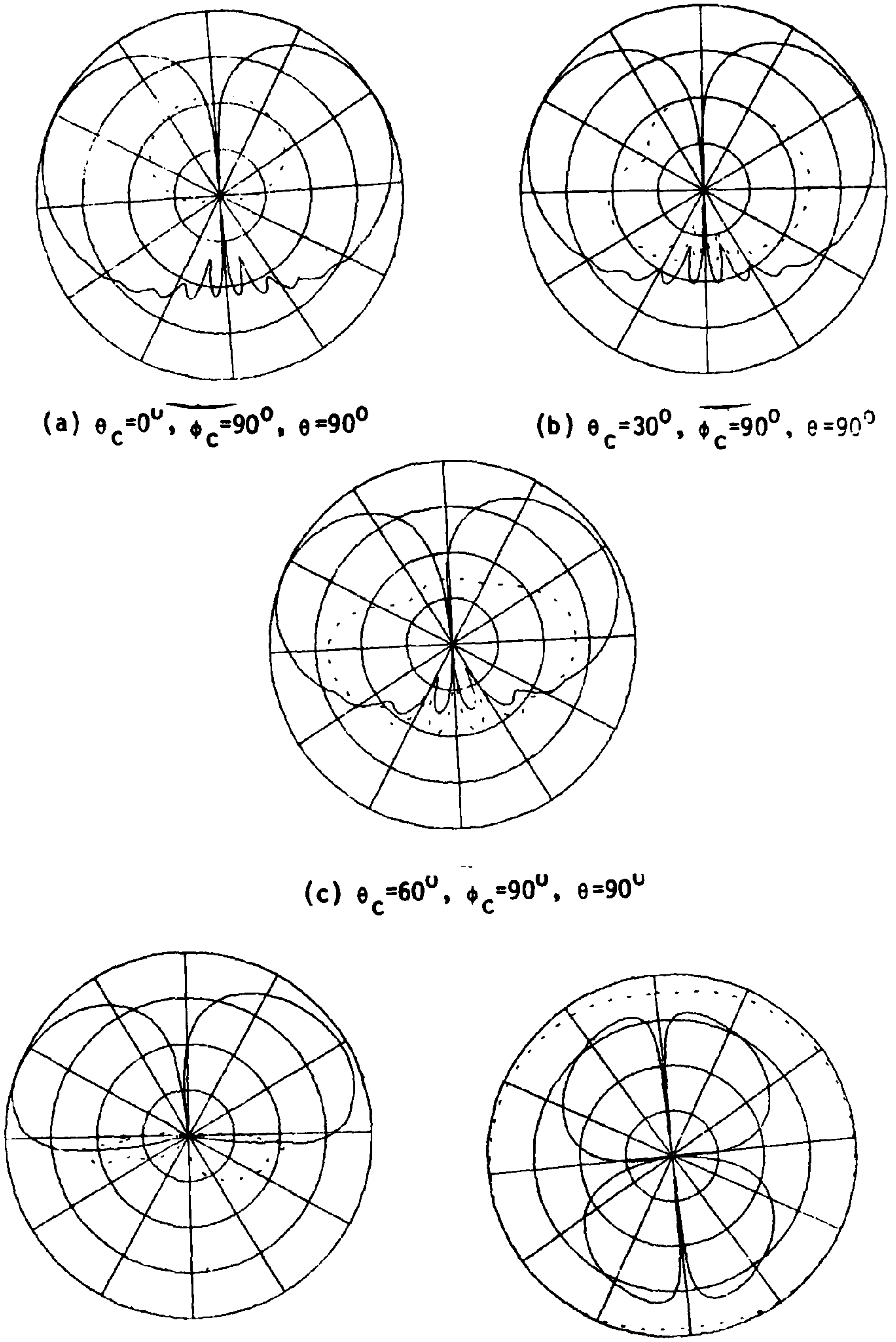

(a) $\theta_c=0^\circ$, $\phi_c=90^\circ$, $\theta=90^\circ$

(b) $\theta_c=30^\circ$, $\phi_c=90^\circ$, $\theta=90^\circ$

(c) $\theta_c=60^\circ$, $\phi_c=90^\circ$, $\theta=90^\circ$

(d) $\theta_c=90^\circ$, $\phi_c=90^\circ$, $\theta=90^\circ$

(e) $\theta_c=90^\circ$, $\phi_c=0^\circ$, $\theta=90^\circ$

Figure 17. Near zone radiation patterns for $R_t=15\lambda$ for a short monopole mounted at $\theta_s=60^\circ$ on a $2\lambda \times 10\lambda$ spheroid.

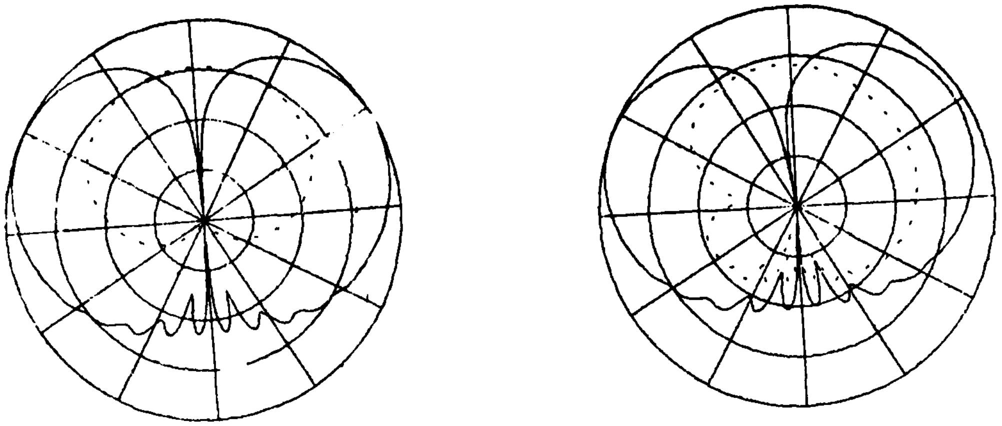

(a) $\theta_c=0^0$, $\phi_c=90^0$, $\theta=90^0$ (b) $\theta_c=30^0$, $\phi_c=90^0$, $\theta=90^0$

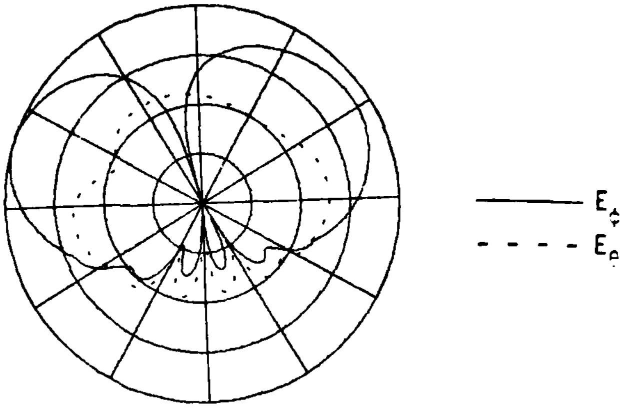

(c) $\theta_c=60^0$, $\phi_c=90^0$, $\theta=90^0$

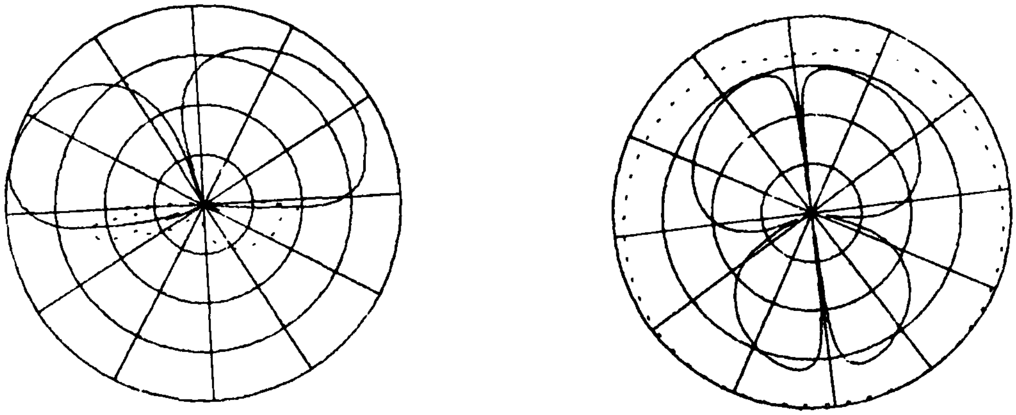

(d) $\theta_c=90^0$, $\phi_c=90^0$, $\theta=90^0$ (e) $\theta_c=90^0$, $\phi_c=0^0$, $\theta=90^0$

Figure 18. Near zone radiation patterns for $R_t=15\lambda$ for a short monopole mounted at $\theta_s=30^0$ on a $2\lambda \times 10\lambda$ spheroid.

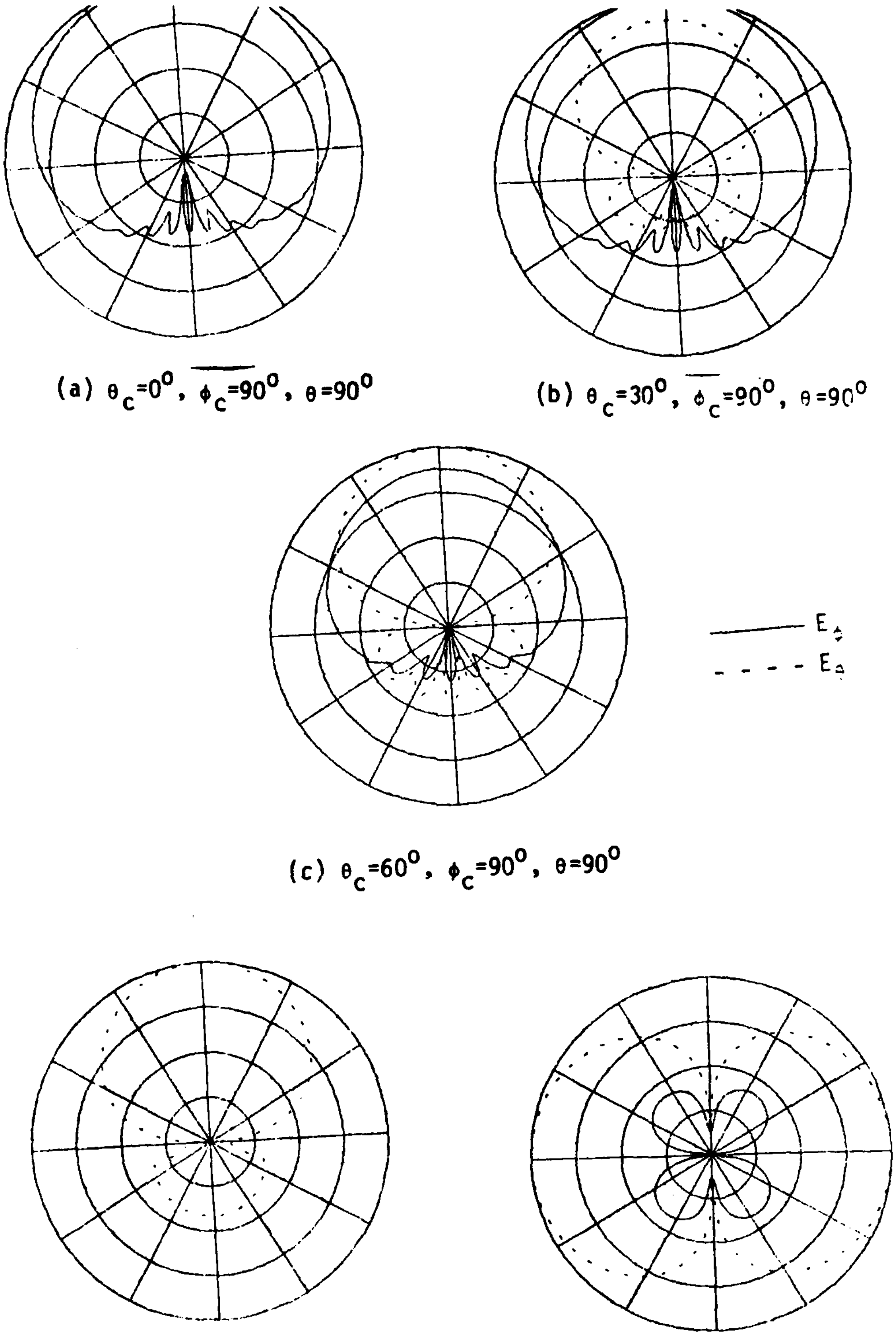

(a) $\theta_c=0^0$, $\overline{\phi_c=90^0}$, $\theta=90^0$

(b) $\theta_c=30^0$, $\overline{\phi_c}=90^0$, $\theta=90^0$

(c) $\theta_c=60^0$, $\phi_c=90^0$, $\theta=90^0$

(d) $\theta_c=90^0$, $\phi_c=90^0$, $\theta=90^0$

(e) $\theta_c=90^0$, $\phi_c=0^0$, $\theta=90^0$

Figure 19. Near zone radiation patterns for $R_t=15\lambda$ for an axial slot mounted at $\theta_s=90^0$ on a $2\lambda \times 10\lambda$ spheroid.

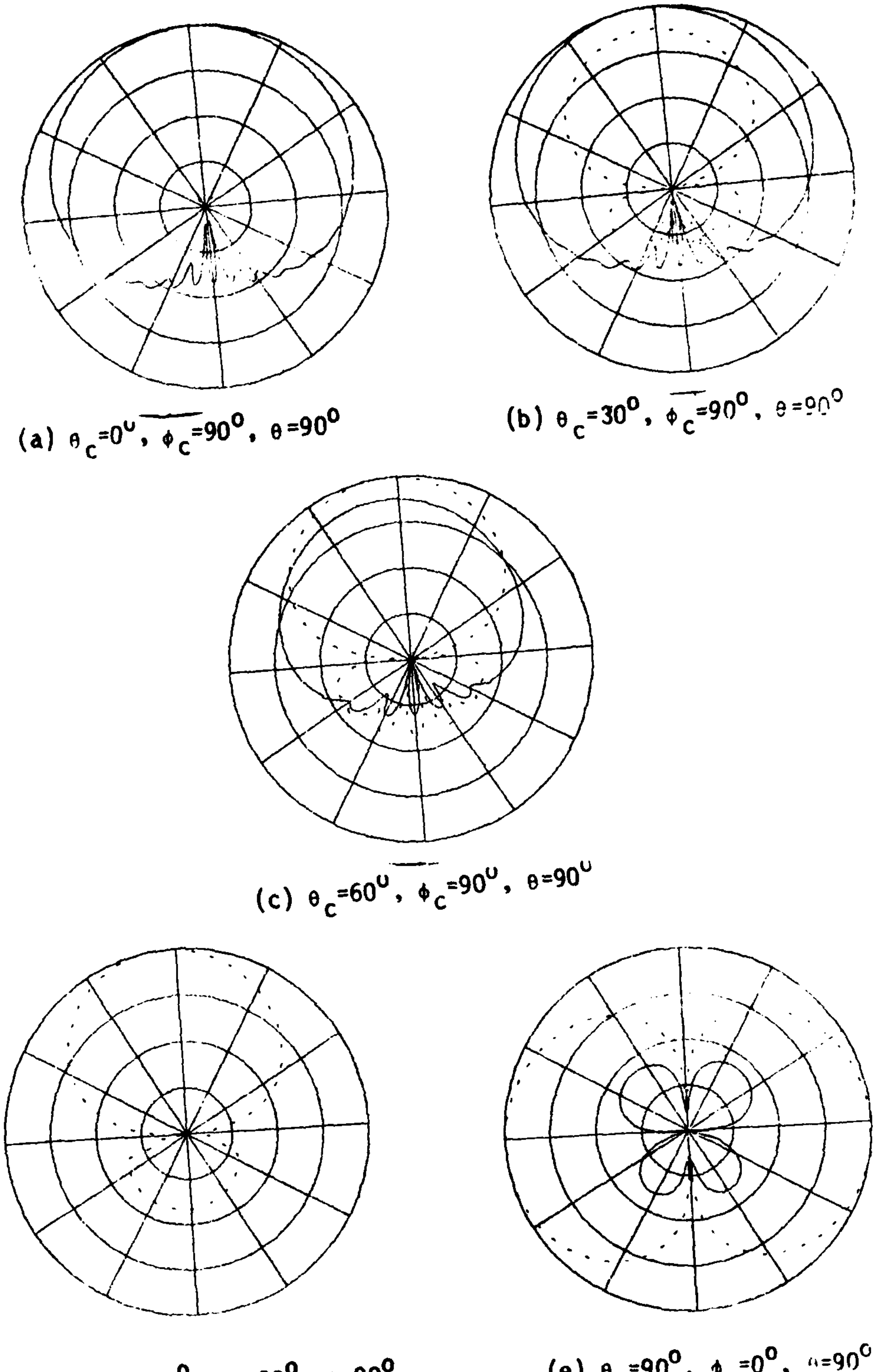

(a) $\theta_c=0^0$, $\phi_c=90^0$, $\theta=90^0$

(b) $\theta_c=30^0$, $\phi_c=90^0$, $\theta=90^0$

(c) $\theta_c=60^0$, $\phi_c=90^0$, $\theta=90^0$

(d) $\theta_c=90^0$, $\phi_c=90^0$, $\theta=90^0$

(e) $\theta_c=90^0$, $\phi_c=0^0$, $\theta=90^0$

Figure 20. Near zone radiation patterns for $R_t=15\lambda$ for an axial slot mounted at $\theta_s=60^0$ on a $2\lambda \times 10\lambda$ spheroid.

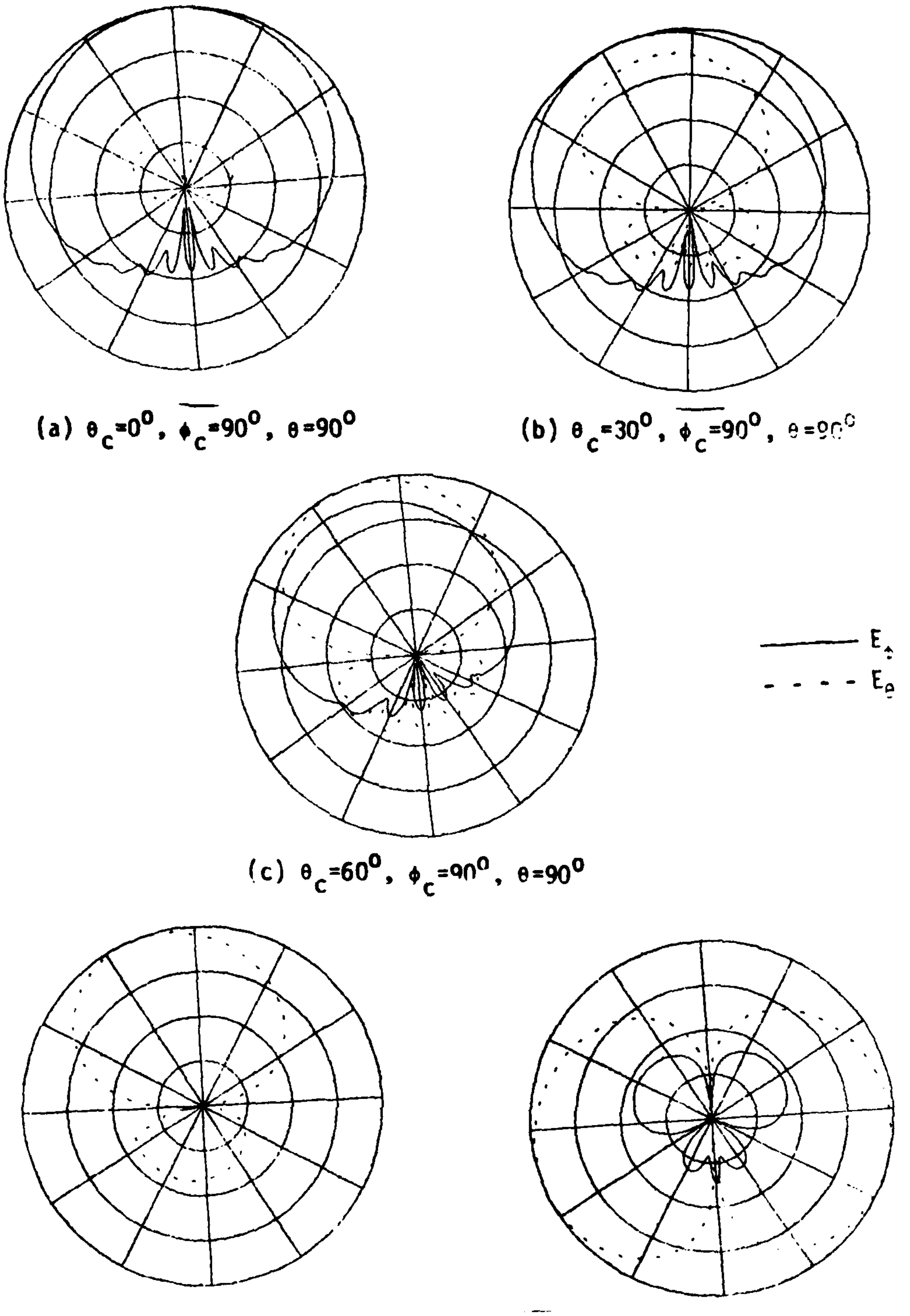

(a) $\theta_c=0^0$, $\phi_c=90^0$, $\theta=90^0$

(b) $\theta_c=30^0$, $\phi_c=90^0$, $\theta=90^0$

(c) $\theta_c=60^0$, $\phi_c=90^0$, $\theta=90^0$

(d) $\theta_c=90^0$, $\phi_c=90^0$, $\theta=90^0$

(e) $\theta_c=90^0$, $\phi_c=0^0$, $\theta=90^0$

Figure 21. Near zone radiation patterns for $R_t=15\lambda$ for an axial slot mounted at $\theta_s=30^0$ on a $2\lambda \times 10\lambda$ spheroid.

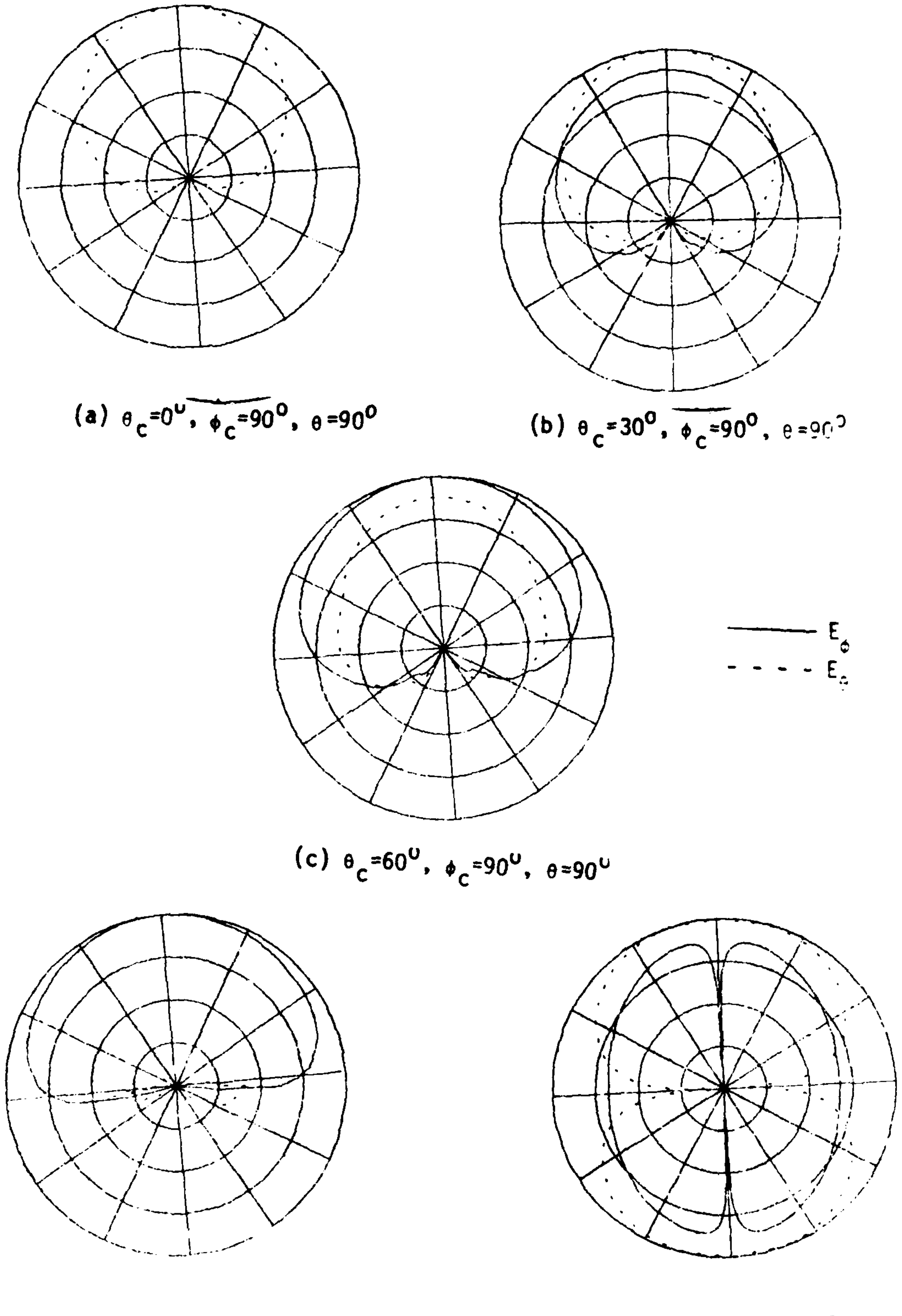

(a) $\theta_c=0^0$, $\phi_c=90^0$, $\theta=90^0$

(b) $\theta_c=30^0$, $\phi_c=90^0$, $\theta=90^0$

(c) $\theta_c=60^0$, $\phi_c=90^0$, $\theta=90^0$

(d) $\theta_c=90^0$, $\phi_c=90^0$, $\theta=90^0$

(e) $\theta_c=90^0$, $\phi_c=0^0$, $\theta=90^0$

Figure 22. Near zone radiation patterns for $R_t=15\lambda$ for a circumferential slot mounted at $\theta_s=90^0$ on a $2\lambda x10\lambda$ spheroid.

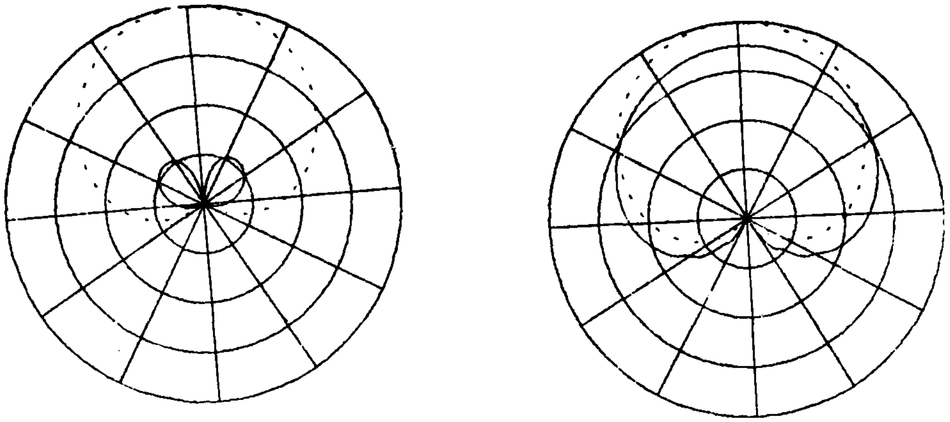

(a) $\theta_c=0^0$, $\phi_c=90^0$, $\theta=90^0$ (b) $\theta_c=30^0$, $\phi_c=90^0$, $\theta=90^0$

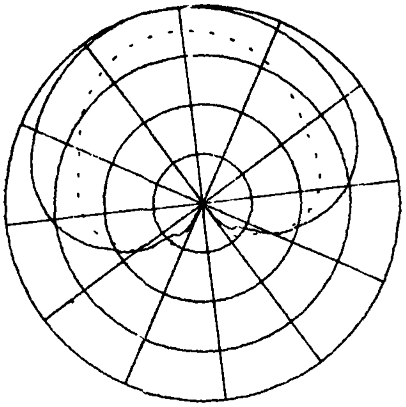

(c) $\theta_c=60^0$, $\phi_c=90^0$, $\theta=90^0$

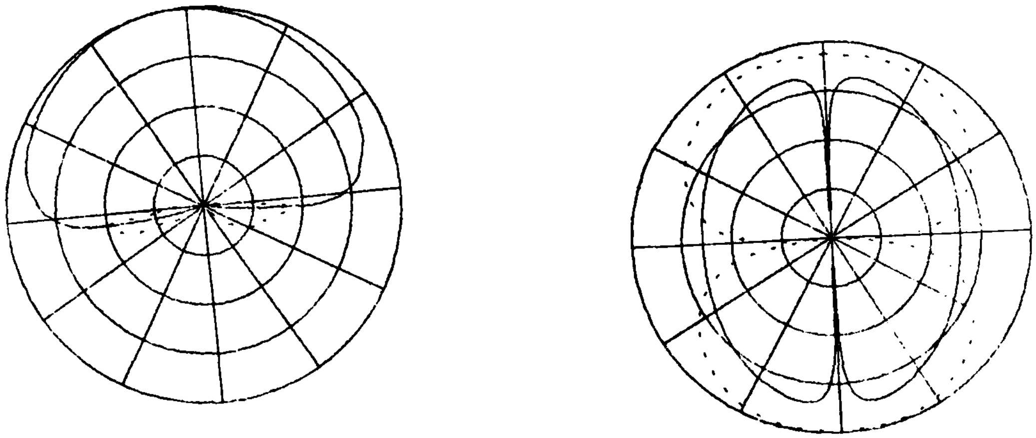

(d) $\theta_c=90^0$, $\phi_c=90^0$, $\theta=90^0$ (e) $\theta_c=90^0$, $\phi_c=0^0$, $\theta=90^0$

Figure 23. Near zone radiation patterns for $R_t=15\lambda$ for a circumferential slot mounted at $\theta_s=60^0$ on a $2\lambda \times 10\lambda$ spheroid.

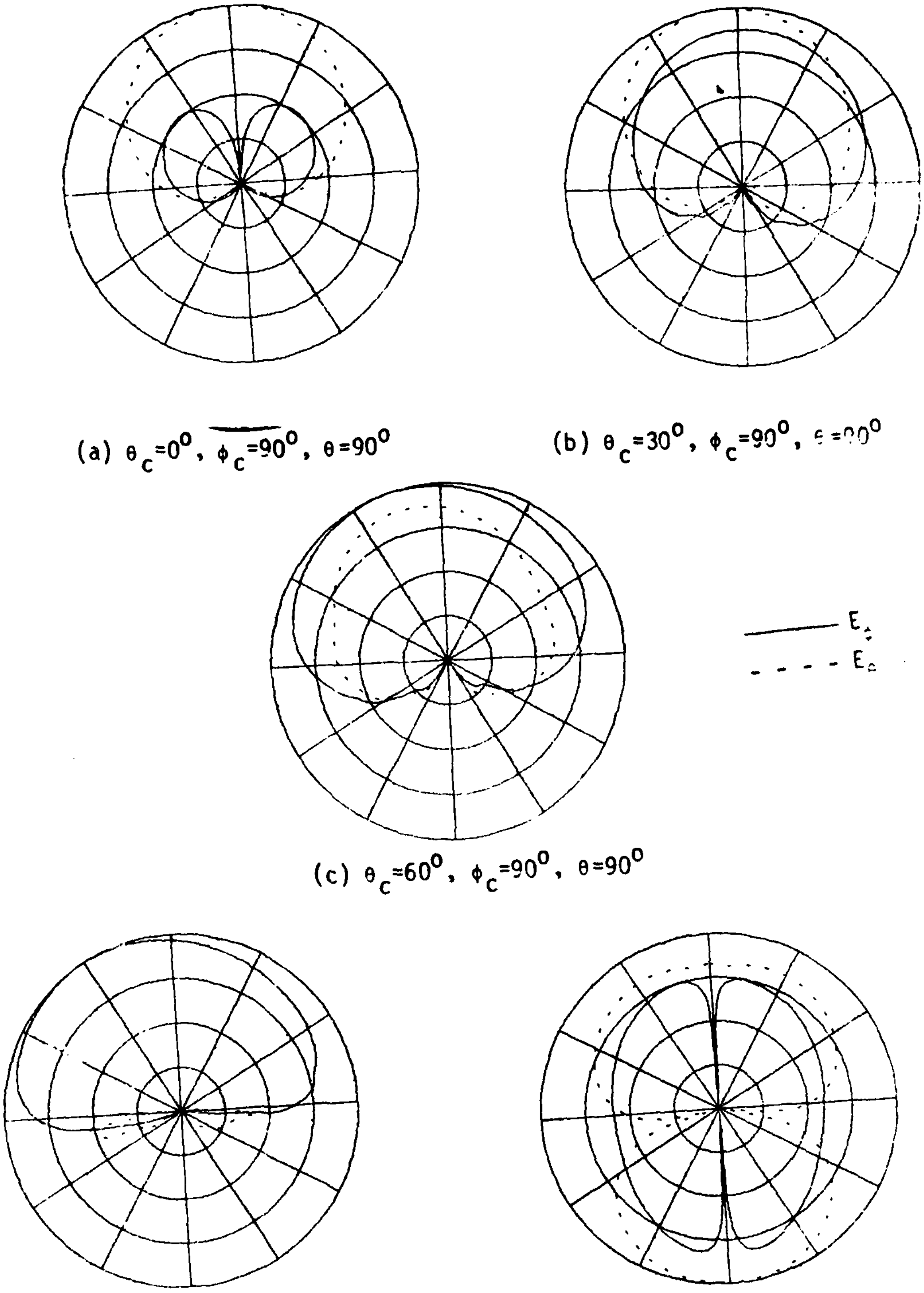

(a) $\theta_c=0^0$, $\phi_c=90^0$, $\theta=90^0$

(b) $\theta_c=30^0$, $\phi_c=90^0$, $\theta=90^0$

(c) $\theta_c=60^0$, $\phi_c=90^0$, $\theta=90^0$

(d) $\theta_c=90^0$, $\phi_c=90^0$, $\theta=90^0$

(e) $\theta_c=90^0$, $\phi_c=0^0$, $\theta=90^0$

Figure 24. Near zone radiation patterns for $R_t=15\lambda$ for a circumferential slot mounted at $\theta_s=30^0$ on a $2\lambda \times 10\lambda$ spheroid.

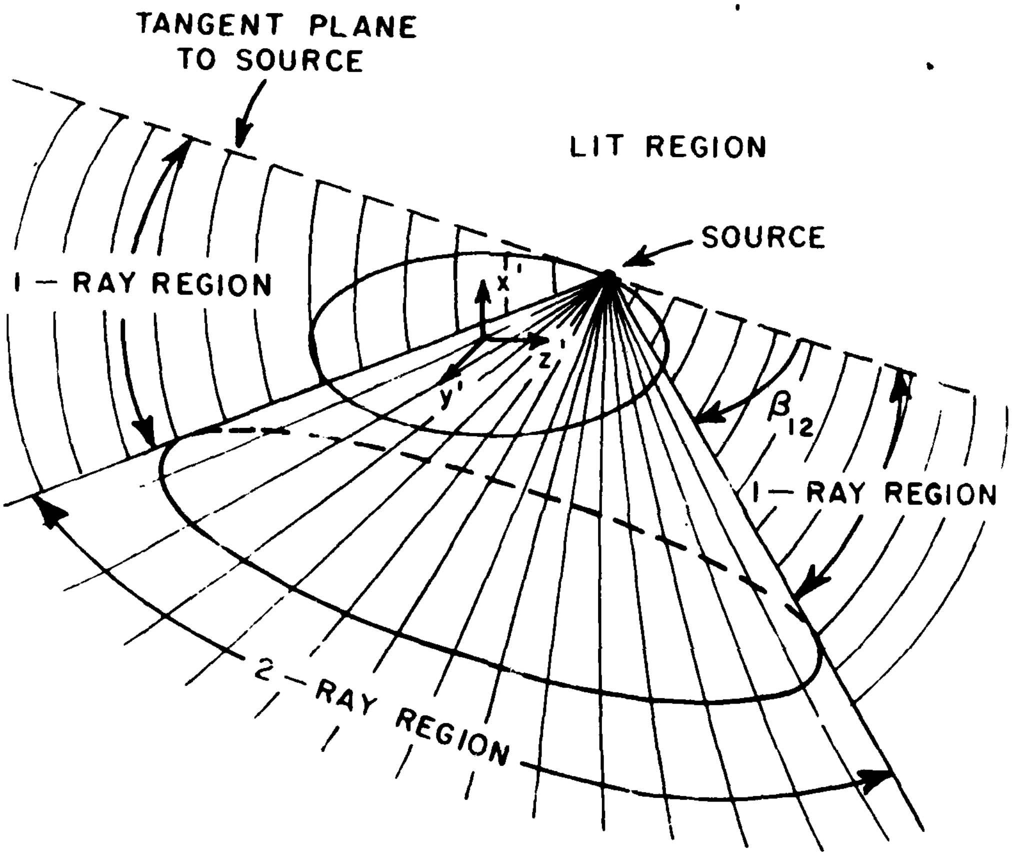

Figure 25. Cone boundary used to define terms to be included in the shadow region.

V. SUMMARY AND CONCLUSIONS

The object of this study has been to develop an efficient numerical solution for the high frequency near zone radiation patterns of a spheroid-mounted antenna. The Geometrical Theory of Diffraction is used in this study to calculate the radiation patterns. The curved surface diffraction solutions are discussed in Section II, where the creeping wave solutions in the shadow region are of particular interest.

Cylinder and cone perturbation methods are presented in Section III to simulate the geodesic paths on a spheroid, which in turn can be used to model an aircraft or missile fuselage. Because the cylinder and cone are developed surfaces, the geodesic paths can be found on the unfolded planar surface. For a given radiation direction in the shadow region, the geodesic path and final diffraction point on the spheroid can, then, be found via an efficient numerical approach.

The Geometrical Theory of Diffraction is combined with the perturbation methods in section IV to obtain various radiation patterns.

These solutions are very useful in predicting the high frequency radiation patterns for antennas mounted on a spheroid. The cylinder and cone perturbation techniques are highly efficient in approximating the geodesic paths on the spheroid for this problem. Further, this perturbation method can be extended to more general convex surfaces such as ellipsoids.

REFERENCES

1. P. H. Pathak, N. Wang, W. D. Burnside, and R. G. Kouyoumjian, "A Uniform GTD Solution for the Radiation from Sources on a Convex Surface," February 1980, Report 711305-3, The Ohio State University ElectroScience Laboratory, Department of Electrical Engineering, prepared under Contract N00019-78-C-0524 for Department of Navy, Naval Air Systems Command.

2. W. D. Burnside, "Analysis of On-Aircraft Antenna Patterns," August 1972, Report 3390-1, The Ohio State University ElectroScience Laboratory, Department of Electrical Engineering, prepared under Contract No. 62269-72-C-0354 for Naval Air Development Center. Also a Dissertation to The Ohio State University, August 1972.

3. M. M. Lipschutz, Differential Geometry, Schaum's Outline Series, McGraw-Hill Book Co., New York, N.Y. (1969).

FILME

-.8